The Structural Stability of P2-Layered Na-Based Electrodes during Anionic Redox

Jean Vergnet, Matthieu Saubanère, Marie-Liesse Doublet, Jean-marie Tarascon, Jean-marie Tarascon

The Structural Stability of P2-Layered Na-Based Electrodes during Anionic Redox

Jean Vergnet,[1,3] Matthieu Saubanère,[2,3] Marie-Liesse Doublet, [2,3] and Jean-Marie Tarascon[1,3]*

[1]*Collège de France, Chimie du Solide et de l'Énergie, UMR CNRS 8260, Paris, France*
[2]*Institut Charles Gerhardt, CNRS – Université de Montpellier, Place Eugène Bataillon, 34 095 Montpellier, France*
[3]*Réseau Français sur le Stockage Électrochimique de l'Énergie (RS_2E), FR5439, Amiens, France*

Abstract

The need to store an ever increasing amount of renewable energy in a sustainable way has rekindled interest for Na-ion batteries owing to the abundance of Na. Their energy density, lower than Li-Ion, can be enhanced by unlocking anionic redox, as recently reported in Na-deficient *P2*-phases. In contrast to their Li-rich counterparts with *O3* stacking, these Na-deficient *P2*-phases show surprisingly good structural stability during anionic redox. Understanding the fundamental science at work in the relation between O/P stacking and anionic redox reversibility is critical to design stable anionic redox cathodes. Herein, through DFT-based analysis of the model compounds *O2*- and *P2*-$Na_{2/3}Mg_{1/3}Mn_{2/3}O_2$, we show that the anionic redox process corresponds to a highly reversible collective distortion of the oxygen network in P stacking, or to a disproportionation of the oxygen pairs associated with significant voltage hysteresis in O stacking. Based on these findings, we used a magnetic-constrained DFT methodology to quantitatively predict the composition range of the reversible cycling that we successfully extend to other Mn-based cathodes ($Na_{2/3}Zn_{1/3}Mn_{2/3}O_2$, $Na_2Mn_3O_7$). This article thus provides fundamental understanding, powerful computational methods and practical guidelines to design more stable anionic redox compounds.

matthieu.saubanere@umontpellier.fr

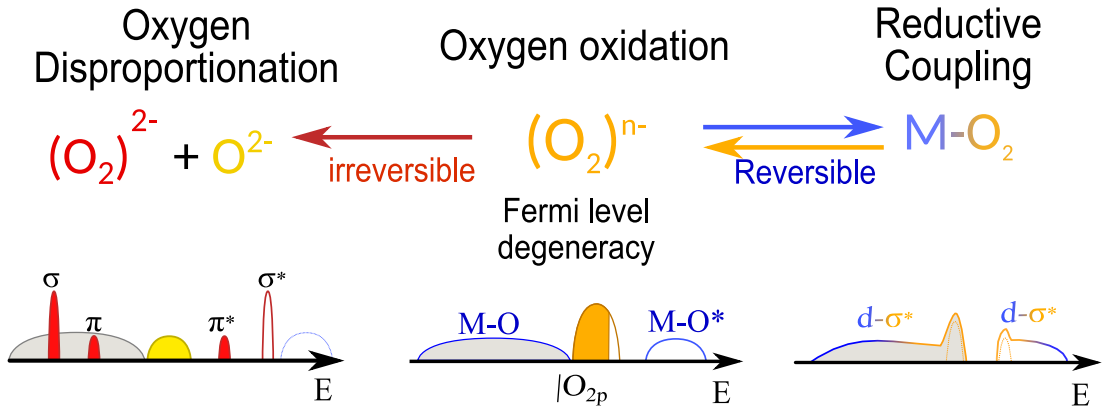

* INTRODUCTION

The development of electric vehicles calls for energy storage with an ever increasing energy density[1]. Today, the most performing Na and Li batteries reach redox potentials that exceed the stability limits of common electrolytes. Therefore, research efforts to reach higher energy density have been oriented towards enhancing capacity rather than potential. Along this line, anionic redox has been the subject of sustained interest since it allows delivering extra capacity. However, voltage decay, sluggish kinetics together with partial irreversibility of oxygen oxidation are major drawbacks that prevent the integration of anionic redox into commercial materials[2]. In order to mitigate these limitations, it is critical to understand the link between structure stability and anionic redox activities in these newly reported Na layered oxides.

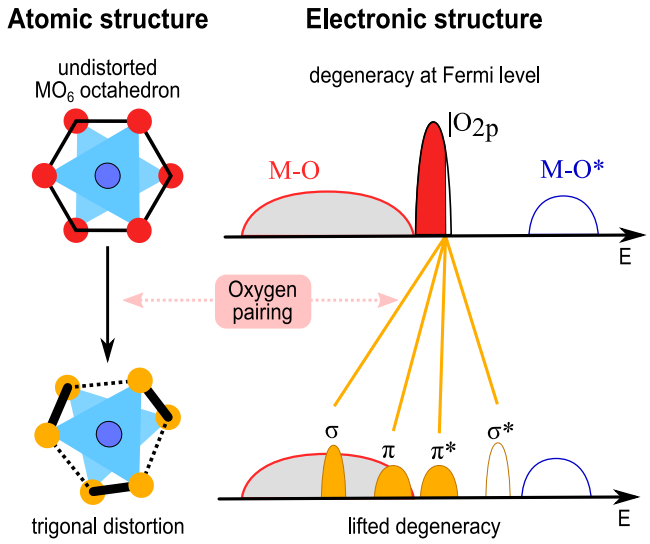

Figure 1: Oxygen oxidation creates a hole in the $|O_{2p}$ band (top). The Fermi level degeneracy in this localized band is unstable (purple line). Oxygen pairing (distortion) splits the $|O_{2p}$ band thus lifting the degeneracy and stabilizing the structure (bottom).

As of today, there is already a vast amount of theoretical and computational works that describe the mechanism of anionic redox [3–5]. Even though some diverging interpretations and wordings persist, there seems to be an emerging consensus on the electronic description of the core mechanism. Anionic redox in transition metal oxides is now well admitted as arising from the participation of oxygen lone-pair states in the electrochemical activity of the material. Under such conditions, electron removal creates holes in the very narrow $|O_{2p}$ band (highly localized states) rather than in the MO anti-bonding states as in $LiCoO_2$. These holes might get stabilized through the formation of oxygen pairs (distortion) leading to uneven O-O distances in the structure, as observed experimentally[6] and illustrated in fig.1. The formation of short O-O bonds splits the $|O_{2p}$ band into bonding and anti-bonding levels of σ/σ^* and π/π^* character.

Up to now, O_2 release due to anionic redox in Li(Na)-rich layered oxides, showing *O3*-stacking (fig. S1), is always associated to transition metals migration[6–9]. Indeed, in some Li-rich compound (Li_2RuO_3 [10,11],Li-rich NMC[12]) and some Na-rich electrodes (Na_2RuO_3[8]), cation migration and O_2 release happen concomitantly while other compounds such as Li_2IrO_3[9] or Na_2IrO_3[6] do not show any of the two. This correlation does not hold for Na-deficient layered oxides, of formula $Na_{2/3}M'_xMn_{1-x}O_2$ (M' = Mg, Zn, Ni, Li, Fe... x>0.2) which crystallize in *P2* stacking (see Fig. S1 in Supplementary Information). Indeed, these compounds show various structural responses to anionic redox such as cation migration and stacking phase transition to O/P hybrid stacking without any O_2 release nor voltage hysteresis[13–19]. Among them, $Na_{2/3}Mg_{0.28}Mn_{0.72}O_2$ was largely reported to show pure anionic redox in charge while maintaining good structural integrity[19–23]. Thus *P* stacking seems to enhance the reversibility of anionic activity.

The P → O phase transition has already been widely studied because it is a source of structural instability in electrodes showing pure cationic redox[24]. The relative stability of P & O phases is mainly governed by electrostatic effects across the Na interlayer [25–27] which is consistent with the similarity of the TM layer in both structures. Interestingly, for compounds showing anionic redox, the P→O phase transition is postponed to lower Na content than for compounds showing exclusively cationic redox. It occurs respectively at x_{Na} = 0.5 in $Na_{2/3}MnO_2$ (cationic) [14] and x_{Na} = 0.3 in $Na_{2/3}Mg_{1/3}Mn_{2/3}O_2$ (anionic)[20]. Moreover, the fully charged structure of the latter exhibits an unconventional OP4 structure consisting in alternating O-P stacking sequence [22](see Fig. S1 in Supplementary Information).

Thus, the questions of how stable is the material structure upon anionic oxidation and how reversible is the process upon reduction depend critically on the stacking type (*O* or *P*). The relationship between structure stability and anionic redox calls for a better rationalization of the underlying mechanism in these Na-deficient layered phases. First-principles DFT calculations were carried out to provide a thorough analysis of the anionic electrochemical activity in the $Na_xMg_{1/3}Mn_{2/3}O_2$ *O2* and *P2* polymorphs. Results show that anionic activity can be stabilized either by a collective distortion, in *P* stacking, which is quite reversible or by a disproportionation of the oxygen network, in *O* stacking, which entails structural instability. Those mechanisms are then rationalized in terms of band structure stabilization involving different magnetic centers. Based on these findings, we propose a magnetization-constrained DFT (MC-DFT) methodology to determine the critical composition beyond which capacity fading and migration take place and we confront our results with experimental evidences on $Na_xMg_{0.28}Mn_{0.72}O_2$. To assess the transferability and the robustness of the present method, we extend our study to other Mn-based cathode materials, namely $Na_{2/3}Zn_{0.22}Mn_{0.78}O_2$ and $Na_2Mn_3O_7$.

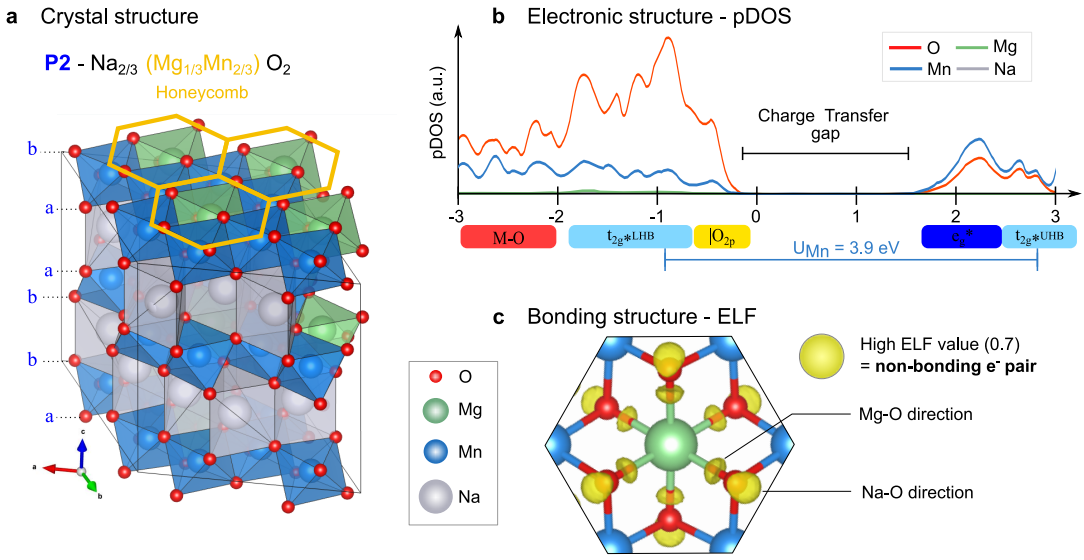

*Figure 2: Characterization of pristine P2-$Na_{2/3}Mg_{1/3}Mn_{2/3}O_2$. **a)** Atomic structure showing P2 stacking and honeycomb ordering of the metal layer. **b)** Atomic projection of the density of states showing a dominant contribution of oxygen states at the Fermi level and a charge-transfer electronic regime. **c)** Electron Localization Function (ELF) of valence electrons: the high value (0.7) isosurface locates the O lone-pairs ($|O_{2p}$ and $|O_{2s}$) between Na-O and Mg-O atoms.*

I. RESULTS

The pristine $Na_{2/3}Mg_{1/3}Mn_{2/3}O_2$ is a *P2* layered compound, meaning that Na^+ ions lie in prismatic sites with a 2 layer periodicity along the c axis. Within the metal layer, Mg and Mn are assumed to be ordered in a honeycomb type arrangement, as shown in Fig. 2a. In this compound, Mn has a +IV oxidation state, in line with the quasi homogeneous Mn-O distances observed in the fully relaxed structure (in contrast to Mn^{+3} which generally displays a strong Jahn-Teller distortion, see Figs. S3 and S4 in Supplementary Information). Its d^3 electronic configuration ($t_{2g}3\ e_g0$) is confirmed by the projected density of states (pDOS) of Fig. 2b, showing that the low-energy t_{2g}*- band is half-filled with unpaired (spin-up) electrons, leading to a local magnetic moment on Mn around $3\mu_B$. The large splitting between the occupied and vacant t2g*-band is known as the Mott gap and arises from the strong electron-electron Coulomb repulsion in the Mn 3d-shell. It leads to an electronic structure in which the occupied t2g*-band lies below the anionic band (see Supplementary Information S3) showing that $Na_{2/3}Mg_{1/3}Mn_{2/3}O_2$ is a charge transfer insulator with a relatively large band gap of about ~1.6 eV. Interestingly, a Crystal Orbital Overlap Population (COOP) analysis [28,29] performed on the pristine material reveals that the electronic states below the Fermi level are pure oxygen states with no orbital mixing with the metal d-orbitals (see Supplementary Information S3). Such non-bonding states are known as

oxygen lone-pair states and their occurrence in transition metal oxides have been extensively discussed in previous works[2,3,5] as arising from M(d)-deficient oxygen environments induced by Li- or Na-excess. Since $Na_{2/3}Mg_{1/3}Mn_{2/3}O_2$ has no Na-excess, the occurrence of oxygen lone-pair states in its electronic structure can be surprising, at first sight. As we recently showed, [30] this apparent ambiguity can be lifted through the computation of the Electron Localization Function (ELF) which is the most standard tool to check to presence of localized lone-pairs in a structure. As shown in Fig.2c, the ELF isosurface computed for the $Na_{2/3}Mg_{1/3}Mn_{2/3}O_2$ structure evidences two distinct lobes on the oxygen pointing towards the Mg^{2+} and Na+ cations. This reveals no significant Mg(s,p)/O(s,p) nor Na(s,p)/O(s,p) orbital mixing indicating that Mg-O and Na-O interactions in this material are purely ionic, whereas Mn/O bond shows some covalency (see fig S4 in supplementary information). It also confirms that anionic redox can occur in conventional transition metal oxides with no alkali-excess, as first reported by P.G. Bruce group[20]. Remarkably, the ELF plot computed for the fully oxidized $Mg_{1/3}Mn_{2/3}O_2$ material shows only one lobe on oxygens, further demonstrating that one of the oxygen lone-pair is involved in the oxidation process (see Fig. S5 in Supplementary Information). The missing oxygen lone-pair is most likely the $|O_{2p}$ since $|O_{2s}$ electrons are much deeper in energy.

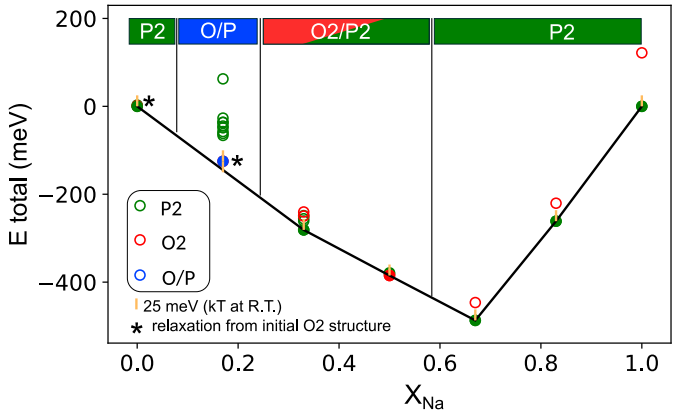

Figure 3: Computed phase stability diagram of P2- and O2- $Na_xMg_{1/3}Mn_{2/3}O_2$. Formation energy of phases obtained from desodiation of the P2 (O2) are shown in green (red), respectively. At low Na content, the O2 structures converting to O/P hybrid stacking or P2 are shown in blue (see computational method). Phases having a formation energy lying on or being near the convex hull are highlighted by filled symbols. It shows a solid solution transition from P2 to O/P stacking hybrid for x_{Na}<0,6. Whatever the starting structure, at x=0, the absence of Na screening leads to P2 stacking with interlayer peroxides.

The phase stability diagram of the *P2*- and *O2*- $Na_xMg_{1/3}Mn_{2/3}O_2$ phases with respect to the biphasic $Na_xMg_{1/3}Mn_{2/3}O_2 \rightarrow x\ Na_1Mg_{1/3}Mn_{2/3}O_2 + (1\text{-}x)\ Mg_{1/3}Mn_{2/3}O_2$ reaction experimentally observed was computed as a function of the sodium composition. It is given in Fig. 3. In perfect agreement with experiments, the *P2* form is thermodynamically favored over the *O2* form for x>2/3 while both polymorphs have equivalent stabilities in the 1/6 < x < 2/3 composition range with relative energies within the room temperature activation energy (~25meV). For x<1/6, the *O2* structure is expected to undergo a partial (x=1/6) or complete (x=0) phase transition to a prismatic stacking, suggesting a P/O intergrowth at low Na content. This result is fully consistent with experimental observations of *O/P* hybrid stacking upon deintercalation [20]. This O/P coexistence needs to be further understood by comparing O and P structures.

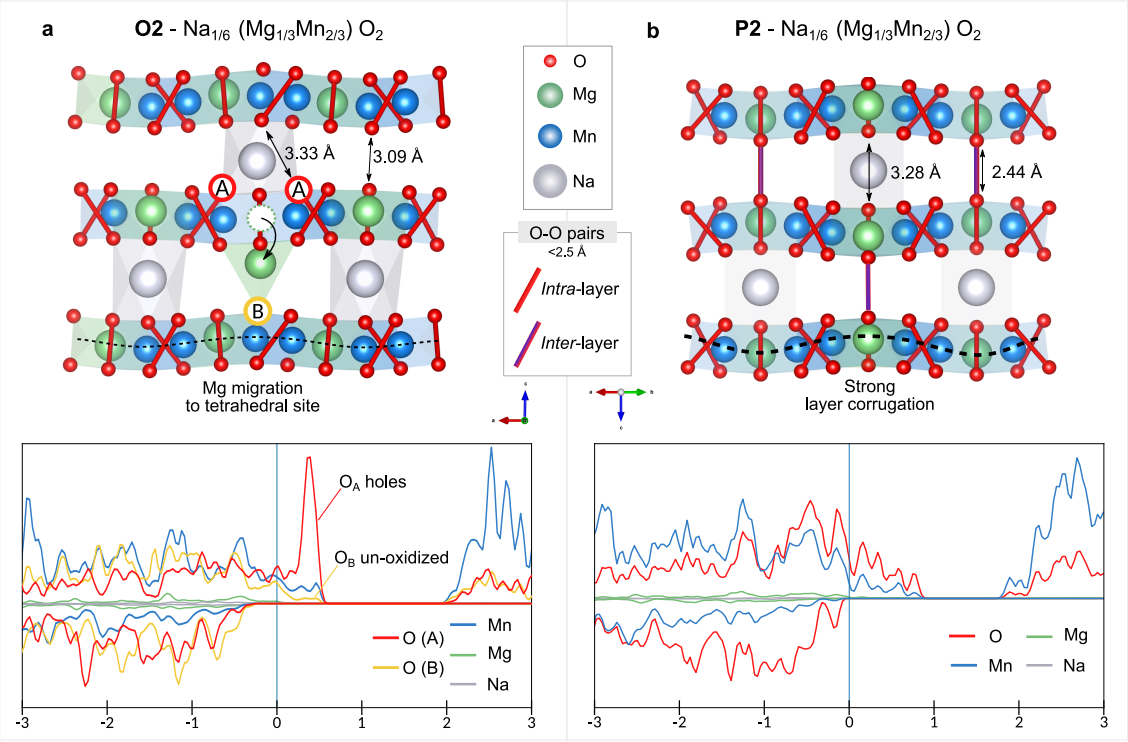

*Figure 4: DFT-relaxed structures of partially desodiated $Na_{1/6}Mg_{1/3}Mn_{2/3}O_2$ (top) for P2 (**a**) and O2 (**b**) stacking types and the corresponding DOS projected on non-equivalent sites. P2 stacking shows homogeneous oxygen oxidation and layer corrugation stabilized by interlayer O-O bonding. In O2 stacking, Mg migration creates oxygens with excess or default of negative charge in their first neighbor shell (A and B). Electron holes concentrate on A oxygens which form pairs (~ $(O_2)^{2-}$) while* B *oxygens have a "full shell" and cannot create O-O pairs (~ O^{2-}).*

Within the whole $0 < x < 2/3$ composition range, our structural relaxations show that both polymorphs conserve their stacking type (*P2* or *O2*) upon desodiation. This means that they correspond to two distinct minima in the potential energy surface of the material that are either far away from each other or separated by large kinetic barriers, thus avoiding a spontaneous transformation from one polymorph to another during the relaxation procedure. This remarkable stability is extremely convenient to investigate the response of each polymorph to desodiation. In both structures, all oxygens form O-O pairs with one next-nearest neighbor while Mn-O bond lengths remain almost constant (see the Mn-O and O-O histograms of Fig. S2 in Supplementary Information). This causes a characteristic trigonal-prismatic distortion of the MnO_6 octahedra which has been used as an experimental signature of oxygen oxidation[8].

At x=1/6, the formation of O-O dimers across the Na layer is observed in the *P2* structure, with O-O distance of 2.5 Å (blue lines in Fig.4). These short O-O interlayer pairs order with Na ions thus inducing a periodic warping of the MO_2 layers. Note that such a layer corrugation was imaged via high resolution microscopy in the fully charged $Na_{2/3-x}Zn_{1/3}Mn_{2/3}O_2$ electrode [31]. This periodic distortion preserves the homogeneity of the oxygen network i.e. each oxygen pair has an equivalent environment and an equivalent oxidation state $(O\text{-}O)^{n-}$ in the *P2* structure.

Interestingly, the *O2* stacking prevents such interlayer O-O pairing at low Na-content, as oxygens no longer face one-another across the Na layer[26]. This is confirmed by our calculations (see Fig. 4 left) and by experiments which both show Mg migration in the Na-layer upon charging the $Na_{2/3}Mg_{1/3}Mn_2 3O_2$ [22,23] and the formation of short O-O distances. As a result of migrations, two oxygen sub-lattices with different environments (and consequently different oxidation states) are created in the *O2* structure. Oxygens close to a Mg vacancy (O_A) have a lack of cationic charges in their first neighboring shell so that their electronic states are raised up in energy and primarily oxidized upon further charge. By analogy, oxygens close to a newly migrated Mg (O_B) have a cationic charge excess in their first neighbor shell so that their electronic states are stabilized in energy and less accessible to oxidation. This is confirmed by our calculations showing a disproportionation of the oxygen network into O_A and O_B at low Na content. The highly oxidized O_A form O_A-O_A dimers within the MX_2 layer (see Fig. 4) with an average oxidation state close to $(O_2)^{2-}$ while the weakly oxidized O_B remains close to O^{2-}. The presence of strongly oxidized species in *O2* type structure obviously questions its stability versus O_2 gas release. By comparing the enthalpy of the O_2 release reaction ΔH_{O2} for both *O2* and *P2* $Na_xMg_{1/3}Mn_{2/3}O_2$ polymorphs (see section Methods and Fig. S7 in Supplementary Information) we confirm that *O* structures are more prone to oxygen release than *P* at low Na content which is again in agreement with the general trends observed experimentally.

Altogether, these results show that *O2* and *P2* $Na_xMg_{1/3}Mn_{2/3}O_2$ polymorphs undergo different anionic redox mechanisms at low Na content: a collective distortion in *P*-structures and an

oxygen disproportionation in *O*-structures. As we will see now, these two mechanisms involve completely different reorganizations of the electronic band structure of the material that could easily be predicted by simple magnetic measurements.

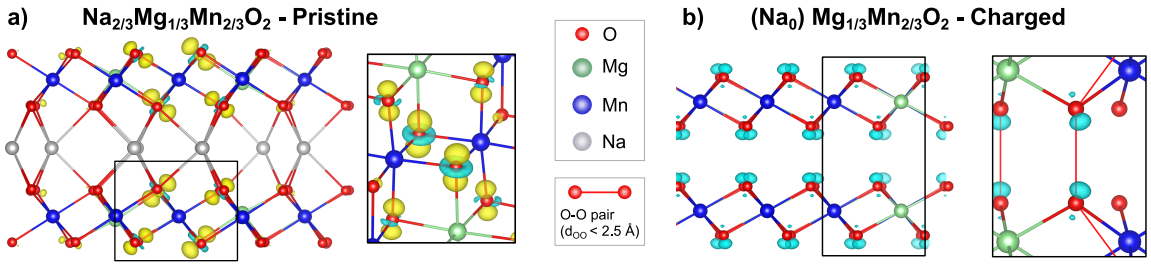

Figure 5: Fukui functions of pristine and charged $Na_xMg_{1/3}Mn_{2/3}O_2$. The electronic reorganization upon addition or removal of 1 electron at constant structure causes an increase (blue) or a decrease (yellow) in the electronic density. ***a)*** *Fukui – of the pristine compound (1 electron removed).* ***b)*** *Fukui + of the fully charged compound (1 electron added). Both isosurfaces have values of 2.10^{-3}. Insets : close-up on oxygen pairs. See Methods section for further details.*

From a fundamental point of view, a significant reorganization of the crystal structure is (most often) the signature of an electronic instability. In the present case, the electronic instability is due to the creation of O-holes in the strongly localized $|O_{2p}$ band of the $Na_{2/3}Mg_{1/3}Mn_{2/3}O_2$ material when Na is removed. This is confirmed by the Fukui – function computed for the pristine material (see Fig.5a) showing that the highest occupied electronic levels of the sodiated structure are pure oxygen orbitals pointing in the Mg-O-Na direction. Given that the pristine structure is built on one single oxygen network (all oxygen are crystallographically equivalent) the removal of 2/3 Na from the structure corresponds to an average number of hole per oxygen $h^O = 1/3$. This electron count does not correspond to any stable electronic configuration known for oxygen, i.e. oxo O^{2-} ($h^O = 0$), peroxo $(O_2)^{2-}$ ($h^O = 1$), superoxo $(O_2)^-$ ($h^O = 3/2$) or O_2 gas ($h^O = 2$). This leads to an unstable electronic structure with either a partially filled $|O_{2p}$ narrow band when no O-O bonds are formed. (see Fig.6 left and Fig. S8). The easiest route for stabilizing such unfavorable localized O-holes is to form O-O bonds to split the partially-filled band into fully occupied and fully empty novel bands. This is precisely the effect of the collective distortion in *P*-structure and the oxygen disproportionation in *O*-structure. As illustrated in Fig. 6 (center panel), the collective distortion involves the metallic Mn(d) orbitals in the process while the oxygen disproportionation does not. The collective distortion (Fig.6 right) arises from a lowering of symmetry due to the formation of short O-O bonds which enables an efficient coupling between the empty (M-O)* states and the partially filled (O-O) σ* states. This orbital

mixing splits the partially-occupied σ* band of the O–O pairs into one occupied and one empty d-σ* bands. The mixing between occupied σ* states and empty (M-O)* states, with a dominant Mn(d) character, increases the formal electron count on the metal. In the rest of the article, this electronic rearrangement, responsible for the collective distortion, will therefore be referred as the reductive coupling mechanism (RCM), as previously coined[8]. As extensively discussed in previous papers [10,30], this mechanism is expected to be reversible as long as the d-σ* empty band remains lower in energy than the first empty (M-O)* band, i.e. as long as they remain the first empty states to be reduced in discharge. With the onset of Mg migration, the disproportionation redistributes the O-holes into the newly formed $(O_2)^{2-}$ peroxides of the O_A-sublattice, leaving the O_B-sublattice almost intact as O^{2-}. This leads to a stable electronic band structure in which the fully filled $|O_{2p}$ band and fully empty σ* band correspond to the weakly oxidized $O^{2-}{}_B$ species and highly oxidized peroxo $(O_A)_2^{2-}$ species, respectively (Fig. 4 left). The formation of the $(O_A)^{2-}$ species is confirmed by the Fukui function computed for the fully charged material and showing that the lowest unoccupied electronic levels involved in the reduction process correspond to the sigma-type orbitals localized on the shortest O-O bonds (see Fig. 5b). According to the COOP analysis of fig. S3, these states correspond to antibonding O-O electronic levels, hence confirming oxygen disproportionation in the fully desodiated phase.

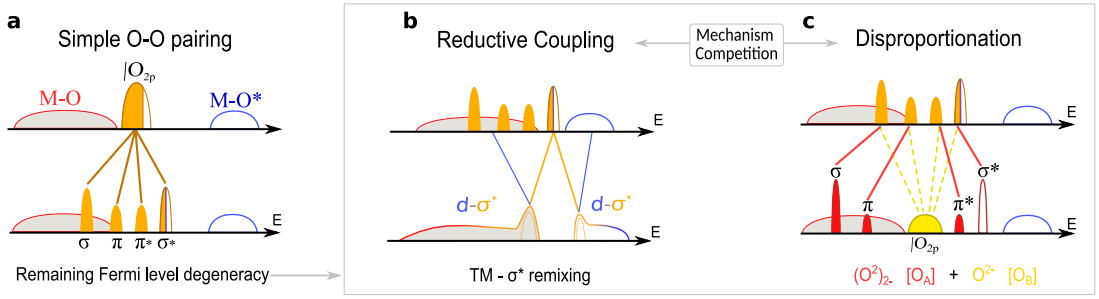

*Figure 6: Possible anionic redox distortion mechanisms. If the number of holes per oxygen h°<1, the simple O-O pairing (**a**) is not sufficient to lift the Fermi level degeneracy thus calling for either of the two other distortions. The reductive coupling mechanism (**b**) opens a gap at the Fermi level through a σ*-t_{2g}* interaction. Without σ*-t_{2g}* interaction, oxygen pairs disproportionate (**c**) into peroxo-like pairs (O_A) and oxo-like atoms (O_B) so that the Fermi level lies below the empty σ*.*

By analyzing the origin of the structural instability upon anionic redox, we were able to qualitatively rationalize the contrasting behaviors of *O* and *P* structure and to correlate the structural changes induced by Na removal to the modification observed in the electronic structure of the O and P polymorphs. This allowed us to understand the importance of *O2* vs. *P2* stacking type on the anionic redox distortion mechanism : *P2* stacking favors a RCM linked

to a reversible collective distortion whereas in *O2* stacking the disproportionation induces migrations which facilitate oxygen release.

Thanks to this analysis, we are now able to identify a quantitative descriptor, namely the total magnetization of the cell, to predict which mechanism is expected to take place as a function of the Na content.

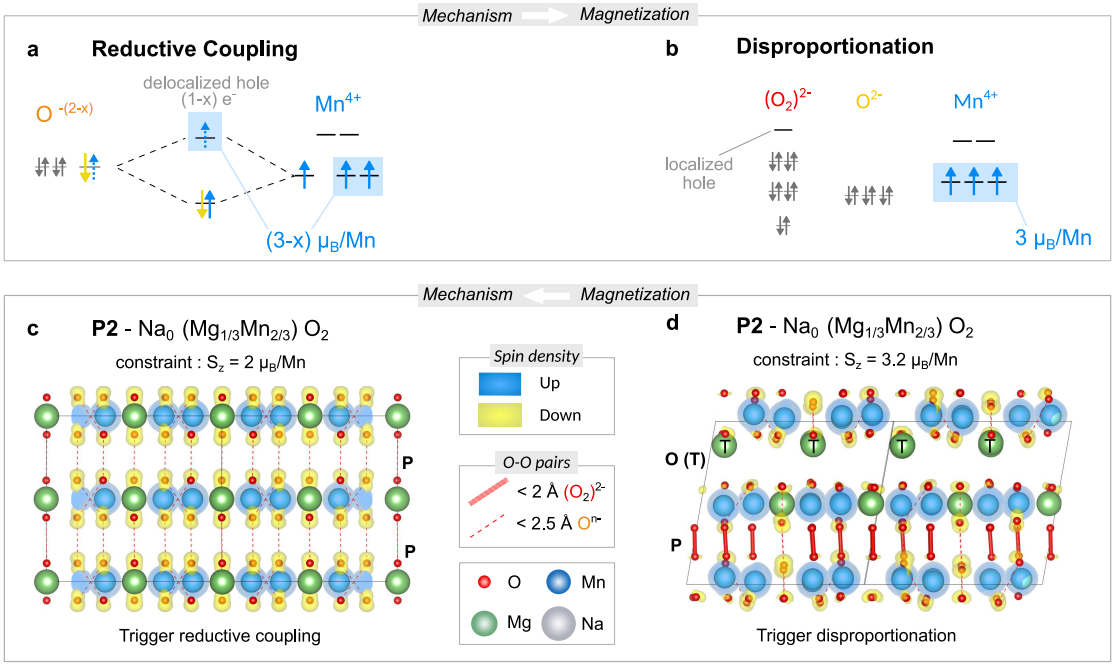

*Figure 7: Top : Schematic orbital interaction in the reductive coupling (**a**) and disproportionation (**b**) mechanisms leading to distinct average magnetizations. Bottom : Structure and magnetization densities of fully charged P2-$Na_0Mg_{1/3}Mn_{2/3}O_2$ relaxed under constrained $\langle S_z \rangle$ showing distinct anionic redox mechanisms. (**c**): $\langle S_z \rangle = 2\ \mu_B/Mn$: the very symmetric structure undergoes RCM. (**d**): $\langle S_z \rangle = 3\ \mu_B/Mn$: this magnetization enlists oxygen disproportionation into ($\sim O_2^{2-}$) and ($\sim O^{2-}$) along with Mg migration in tetrahedral sites (T), thus leading to mixed O/P stacking. Some Mn are reduced to +3 (see figs. S9 and S10).*

In the case of the reductive coupling mechanism (RCM), the unpaired electrons of oxidized oxygens get partially paired with unpaired electrons of the Mn magnetic center (high-spin state) through the covalent Mn-(O-O) interaction and the creation of d-σ* states (see Fig. 7.a). Compared to the pristine material, the total magnetization of the unit cell $\langle S_z \rangle$ should thus decrease linearly with the concentration of oxygen hole or equivalently with the amount of removed sodium. In that case, oxygens bearing unpaired electrons are magnetic centers as demonstrated by the magnetization density displayed in Fig.7.c and already evidenced through

EPR measurements in other cathode materials displaying anionic redox such as $Li_2Ru_{0.75}Sn_{0.25}O_3$[32].

In the case of disproportionation (Fig. 7.b), since both oxo- O^{2-} and peroxo- $(O_2)^{2-}$ are closed-shell and non-magnetic species, the total cell magnetization $\langle S_z \rangle$ corresponds to that of the Mn^{4+} magnetic center and should remain equal to that of the pristine material. Note that an increase of the total magnetization is only expected when, for charge balance, the formation of O_2^{2-} and/or O_2 release enlists a reduction of neighboring Mn^{4+} ($3\mu_B$) into Mn^{+3}($4\mu_B$) (Fig. S10).

Taking advantage on these observations, we can evaluate which mechanism takes place in a material by simply following the lowest energy pathway on the spin-dependent energy landscape of the material. The total energy of the $Na_xMg_{1/3}Mn_{2/3}O_2$ material was thus computed as a function of x and total magnetization of the cell (see section Methods). Note, that such analysis provides experimentalists with new means to distinguish which mechanism is involved in the oxygen activity by looking at the magnetic properties of the discharged phase.

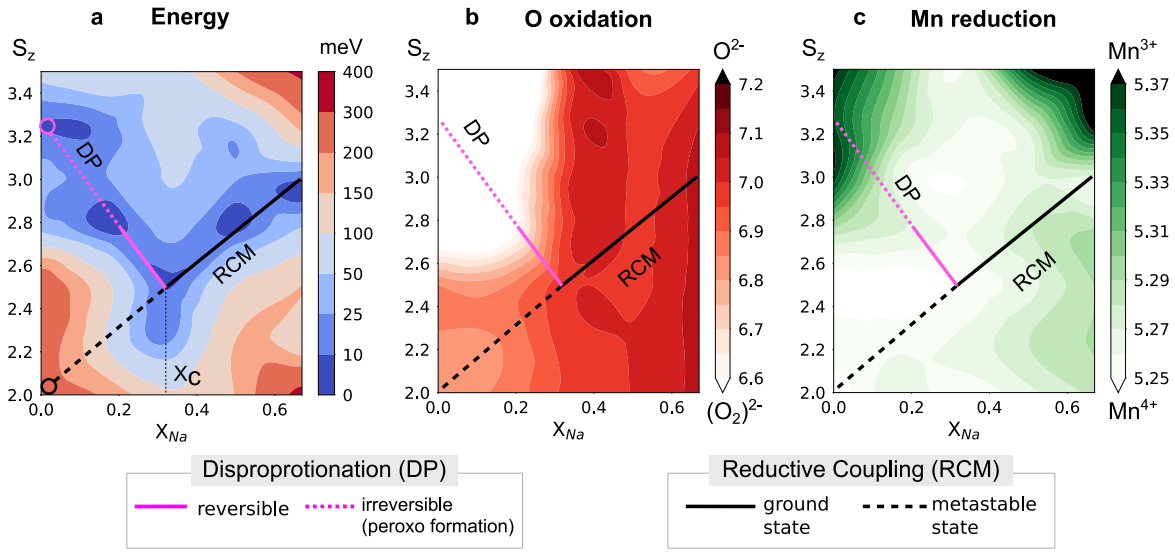

*Figure 8: **a)** Energy landscape computed for $Na_xMg_{1/3}Mn_{2/3}O_2$ as a function of x and for various cell magnetizations. The energy scale is given on the right part of the figure with the lowest energy in blue and highest energy in red. **b)** et **c)** Atomic net population evolution as a function of x for the most oxidized oxygen and the most reduced manganese computed from a Bader analysis. The Bader populations of oxidized and reduced species are indicated on the right part of the picture and scaled with respect to those of reference species with known formal oxidation states.*

Results are presented in fig. 8.a. Starting from x = 2/3 in which the manganese is the only magnetic center, the total magnetization of the cell is maximum ($\langle S_z \rangle = 3$, all Mn^{4+} in high spin configuration). When removing Na, a linear decrease of $\langle S_z \rangle$ (solid black line) is observed, indicative of a RCM. The decrease in $\langle S_z \rangle$ is pursued down to a critical Na composition of ca. 0.3 where the total magnetization is $\langle S_z \rangle = 2.5$. Below this critical Na content, the total magnetization along the lowest-energy path starts to increase (solid pink line), indicating the onset of oxygen disproportionation. In this low Na content region, the RCM (dashed black line) no longer corresponds to the electronic ground state of the material. To characterize the reversibility of the disproportionation, we monitor the appearance of peroxides and Mn^{3+} via atomic charge analysis (Bader net population, see section Methods). For each structure, the charge of the most oxidized oxygen and the most reduced Mn are compared to those of O^{2-}/O_2^{2-} in Fig. 8b and Mn^{3+}/ Mn^{4+} in Fig. 8c. The central region corresponding to the reductive coupling mechanism (RCM) is characterized by a smooth oxidation of the oxygen and a constant charge on Mn. Conversely, the upper left corner corresponding to the oxygen disproportionation (Dp) highlights a strong oxidation of oxygen. Below a composition threshold of x=0.15, the oxygen charge becomes lower than that of peroxides in Li_2O_2 (white zone in Fig. 8b) and Mn get reduced to Mn^{3+}. This corresponds to a limit of Na composition below which O_2 release is expected to occur, therefore making the anionic process in charge irreversible in discharge. This limit is indicated on Fig.8b by the dashed pink line while the solid pink line corresponds to the crossover from the RCM to a weak, yet reversible disproportionation, accompanied with migration and *O→P* phase transition ($0.15<x<0.3$). To confirm the occurrence of this crossover regime at $x_{Na}=1/6$, featuring both the RCM and some disproportionation, and to visualize the shape of the orbitals involved we plotted the partial electronic charge obtained by integrating the square of the Kohn-Sham wave function at different energy range for the pristine and the desodiated phase (see Fig. S13 & S14 in SI respectively). We thereby confirmed that the *P2*-$Na_{1/6}Mg_{1/3}Mn_{2/3}O_2$ displays the electronic signature of both mechanisms, thus validating the occurrence of a crossover region.

This landscape sheds light on experimental data indicating the formation of O/P-hybrid stacking phase for $Na_xMg_{1/3}Mn_{2/3}O_2$ at low Na content[20]. Indeed, real compounds tend to display a mixed stacking (OP4 phase, see fig. S1 & S11 in supplementary information) over a pure P2 or O2 as a compromise between electrostatic stabilization, which favors O stacking, and interlayer hole delocalization, which occurs in P stacking. Relaxation of an OP4 cell at $x_{Na}=1/6$ (fig. S11) confirms that the small amount of electrons removed from the oxygen is localized around the prismatic inter-layers O-O pairs and that oxygens in the remaining octahedral stacking are not sufficiently oxidized to trigger Mg migration. It means that the two types of distortions coexist below x_c.

At this stage, a remaining question regards the origin of the hysteresis and how the quantification of the competition between collective distortion and oxygen disproportionation can shed more light on this issue. To clarify this point, we plotted the pDOS of the two structures presented in Fig. 7 (and Fig. S12). In case of a disproportionation, the formation of peroxo species leads to a band inversion in the electronic structure of the material (O-O σ^* raise above MO* states). As a consequence, from a static point of view, the discharge process differs from the charge process since MO* should be reduced prior to oxygen. This is at the origin of the hysteresis, as previously evidenced by Gent et al. in Li-rich NMC materials[7].

Interestingly, the RCM regime does not show band inversion (O-O σ^* stays below MO* states). Controlling x_c to keep anionic redox materials in the RCM regime should therefore be a good strategy to avoid voltage hysteresis. This can be achieved by limiting the number of holes per oxygen (h°<1/3 [30]) or by designing materials that can reversibly accommodate the strain induced by the collective distortion without collapsing, such as the beta phase of Li_2IrO_3[6]. It is noteworthy that for a biphasic electrochemical process, if the alkali content of the alkali-poor phase is below x_c, the band inversion and thus the hysteresis occurs as soon as the alkali-poor phase is formed, disregarding the state of charge.

Confronting experiment and generalizing to other compounds

To assess the robustness of our approach, we extend our protocol to the recently proposed Mn-based Na electrodes, $Na_xZn_{1/3}Mn_{2/3}O_2$[31] and $Na_{4/7}Mn_{6/7}O_2$[33] and confront our results to the experimental data.

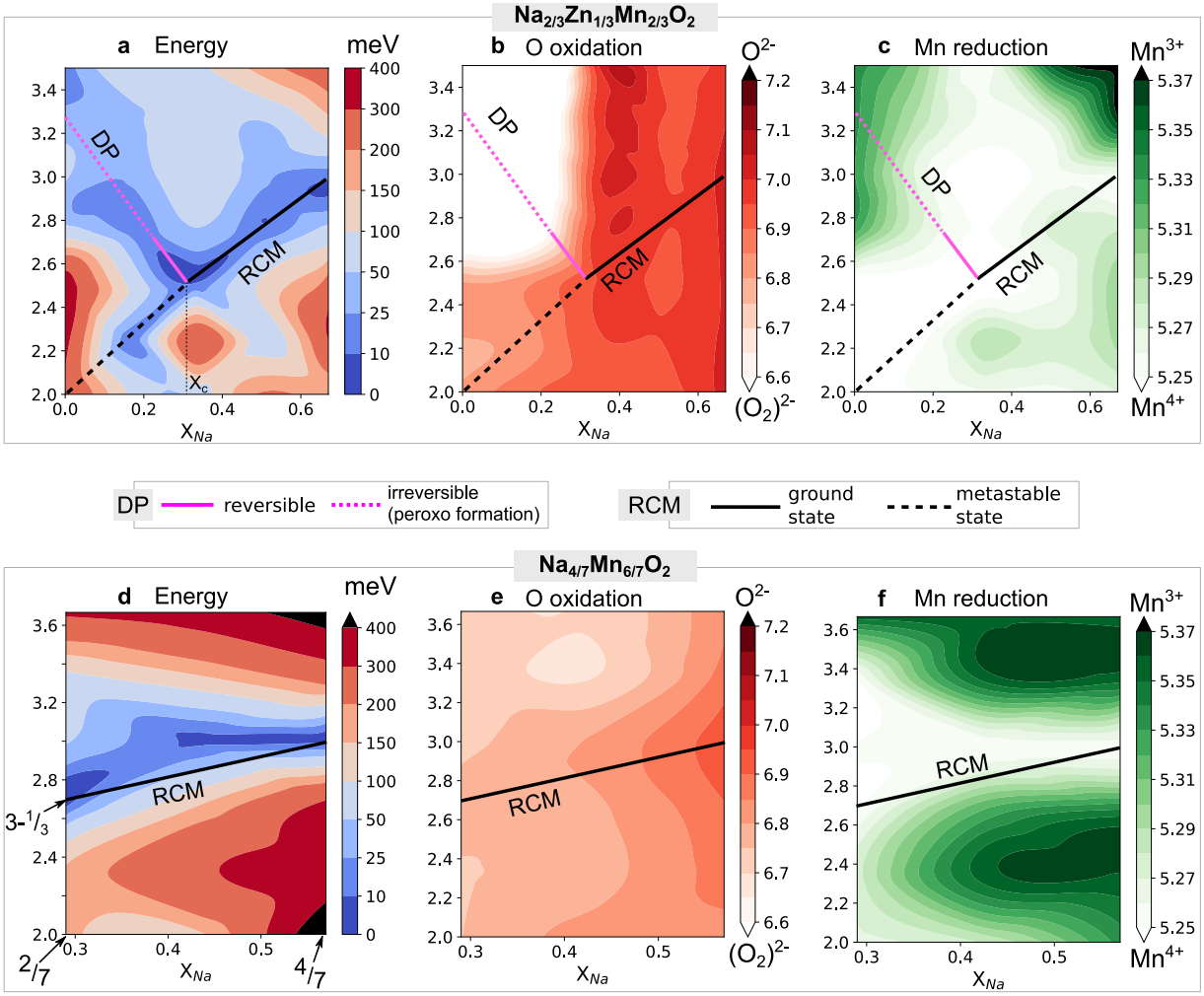

*Figure 9: Energy landscapes, Bader populations of most oxidized oxygen and most reduced Mn of $Na_xZn_{1/3}Mn_{2/3}O_2$ (resp. **a**, **b** & **c**) and $Na_{4/7}Mn_{6/7}O_2$ (resp. **d**, **e** & **f**) (see fig.8 for details).*

Our result shows that $Na_xMg_{1/3}Mn_{2/3}O_2$ and $Na_xZn_{1/3}Mn_{2/3}O2$ display very similar energy landscape with disproportionation taking place at low sodium contents. Thus their electrochemical behavior should also be very similar with a large hysteresis and Mg/Zn migration at the end of charge. This indicates that the nature of the ionic metal, either Mg or Zn does not impact the competition between disproportionation and RCM, in full consistency with

recent reports on P2-$Na_{0.72}Li_{0.24}Mn_{0.76}O_2$ [34], P2- $Na_{0.6}Li_{0.2}Mn_{0.8}O_2$[35] and P3-$Na_{0.6}Li_{0.2}Mn_{0.8}O_2$[36] which all display a voltage hysteresis when anionic redox occurs. On the contrary, the collective distortion is shown to be favored all along the Na removal in $Na_{4/7}Mn_{6/7}O_2$ so that the charge should be perfectly reversible without hysteretic behavior neither capacity fading. These results are in well agreement with experimental data for both the Zn based compound and $Na_xMn_{6/7}O_2$ since for the former a large hysteresis behavior is observed in galvanostatic plot, and accompanied with Zn migrations at the end of charge[31]. In contrast, no hysteresis is observed in galvanostatic plot for $Na_xMn_{6/7}O_2$ [33].

CONCLUSION

In this paper we have studied the anionic redox activity in *P2*-$Na_xMg_{1/3}Mn_{2/3}O_2$ and we have shown that there is a competition between a collective distortion of the lattice and a disproportionation of the oxygen pairs that we characterized by a threshold Na content $x_c = 0.25$. Moreover, we demonstrated that this competition can account for the hysteresis observed in this compound which stems from a stabilization of disproportionation over collective distortion at the end of charge. Taking $Na_xMg_{1/3}Mn_{2/3}O_2$ as an example, we further showed the importance of *O2* vs. *P2* stacking type on the aforementioned competition, with *P2* favoring collective distortion as opposed to *O2*. Lastly, we provided a novel method relying on the link between the stabilization mechanism and the magnetization to determine the range in which the cooperative distortion is favored. Altogether, these findings offer new means to tune hysteresis in materials relying on anionic redox processes by manipulating x_c, hence providing new directions for designing better Na (Li) electrode materials.

METHODS

Structure generation

Starting from experimental *P2* structure obtained by XRD refinement where partial occupancies have been rounded up, *O2* and *OP4* structures were derived by layer gliding using the Python Material Genome library[37]. To obtain the desodiated structures, we iteratively removed the Na nuclei according to their Madelung energy (assuming integer oxidation state for every ion). This technique is less accurate but much faster than the enumeration of all permutations for each composition. Removing two distinct Na site at each iteration (either highest or second highest Madelung energy) allowed to create distinct Na-orders for each Na content. From there we used the structures on (or near) the convex hull to perform further analysis.

DFT

For each Na content, the 5 Na order of lowest electrostatic energy were then relaxed using the *Vienna Ab-Initio Simulation Package* using ultra-soft PAW pseudo-potentials and the Perdew-Burke-Ernzerhof functional with a generalized gradient approximation[38–40]. We added D3 correction to account for the Van Der Waals interaction[41,42] as well as a U_{eff} = 4 eV to account for electron–electron interactions on Mn[43]. The forces on the atoms were converged to 10^{-3} eVÅ^{-1} with a plane-wave energy cut-off of 600 eV and a well converged set of Kpoints.

Analysis

Third party tools

Bader analysis was performed using the code from Henkelman's group[44]. The COOP was computed using LOBSTER code[28]. ELF and PARCHARG files were generated using VASP built-in methods and visualized using VESTA[45].

O_2 release enthalpy

ΔG_{O2} was obtained following ref [5] : we first computed the energy of the O_2 molecule *E(O_2)* corrected with the empirical parameter given by Ceder's group[46]; then for a given relaxed structure of energy *E(initial structure)*, we removed the most oxidized oxygen (lowest Bader population) and computed the energy of the fully relaxed oxygen deficient structure *E(O deficient structure)*. When neglecting the influence of entropy, the O_2 release enthalpy is then given by:

$$\Delta E = [\ E(\text{O deficient structure}) + \tfrac{1}{2}\, E(O_2)\ ] - E(\text{initial structure})$$

Electronic response analysis

Starting from a fully relaxed initial structure, we removed (or added) 1 electron per supercell (containing 24 formula units), performed an electronic relaxation with fixed structure. By

subtracting the corresponding charge density to that of the pristine, we obtained the charge density variation upon oxidation at constant structure.

$$\Delta\rho = \rho \text{ (frozen structure +/- } 1e^{-}\text{)} - \rho\text{(relaxed structure)}$$

Sampling magnetic energy Landscape

When neglecting the weak spin-orbit interaction, Sz becomes a good quantum number. Thus energy minimization yields the ground state of each Sz subspace, thus allowing an efficient sampling of the magnetic energy landscape. Since the Coulomb repulsion in 3d TM leads to high-spin configuration, Sz directly correlates with the number of unpaired electrons when ferromagnetic order is considered. We verified that, energetically speaking, the magnitude of the magnetic exchange coupling J is far lower than the "Hubbard" electron pairing energy U :

$$E_{FM} - EA_{FM} = 10 \text{ meV} << E_{FM} - E_{NM} = 2 \text{ eV (see Fig. S15 in SI)}$$

where E_{AFM} (E_{FM}) refers to the energy of anti-ferro magnetic order (ferromagnetic order), respectively, and E_{NM} is the energy of the non-magnetic electronic ground-state obtained by spin non-polarized calculations. Consequently sampling the energy landscape by constraining Sz around the ferromagnetic solution of the pristine ($3\mu_B$/Mn) allows to study the pairing of holes created when removing Na from the pristine and distinguishing between a localized hole pairing on oxygen (formation of peroxo which does not change the total Sz) and a delocalization of unpaired holes over the M-O bonds which decrease the total Sz (See Fig. 7).

Energy and Bader net populations were computed on relaxed 2*2*1 super-cells of P2-$Na_xMg_{1/3}Mn_{2/3}O_2$ at various compositions under constrained magnetization. Composition (x_{Na}) ranged from 0 to 2/3, by intervals of 1/6. Magnetization (NUPDOWN) ranged from 2 to 3.75 μ_B/Mn by intervals of 0.25. For each composition, we checked that the initial ferromagnetic order on the Mn-sub-lattice was conserved during the relaxation. Landscape was obtained by cubic spline interpolation of these data-points.

Author Contributions :

Conceptualization: M-L.D. M.S., and J-M.T.; Methodology : M.S., J.V.; Investigation, software, vizualization : J.V.; Writing – Original Draft : J.V., M.S.; Writing – Review & Editing : J.V., M.S., M-L.D., and J-M.T.; Resources : M-L.D. (ICGM computing facilities); Supervision : M.S., M-L.D., and J-M.T.

Competing financial interest

The authors declare no competing financial interest.

1. Larcher, D., and Tarascon, J.-M. (2014). Towards greener and more sustainable batteries for electrical energy storage. Nat. Chem. *7*, 19–29.

2. Assat, G., and Tarascon, J.-M. (2018). Fundamental understanding and practical challenges of anionic redox activity in Li-ion batteries. Nat. Energy *3*, 373–386.

3. Seo, D.-H., Lee, J., Urban, A., Malik, R., Kang, S., and Ceder, G. (2016). The structural and chemical origin of the oxygen redox activity in layered and cation-disordered Li-excess cathode materials. Nat. Chem. *8*, 692–697.

4. Okubo, M., and Yamada, A. (2017). Molecular Orbital Principles of Oxygen-Redox Battery Electrodes. ACS Appl. Mater. Interfaces *9*, 36463–36472.

5. Xie, Y., Saubanère, M., and Doublet, M.-L. (2017). Requirements for reversible extra-capacity in Li-rich layered oxides for Li-ion batteries. Energy Environ. Sci. *10*, 266–274.

6. Pearce, P.E., Perez, A.J., Rousse, G., Saubanère, M., Batuk, D., Foix, D., McCalla, E., Abakumov, A.M., Van Tendeloo, G., Doublet, M.-L., et al. (2017). Evidence for anionic redox activity in a tridimensional-ordered Li-rich positive electrode β-Li2IrO3. Nat. Mater. *16*, 580–586.

7. Gent, W.E., Lim, K., Liang, Y., Li, Q., Barnes, T., Ahn, S.-J., Stone, K.H., McIntire, M., Hong, J., Song, J.H., et al. (2017). Coupling between oxygen redox and cation migration explains unusual electrochemistry in lithium-rich layered oxides. Nat. Commun. *8*, 2091.

8. McCalla, E., Abakumov, A.M., Saubanere, M., Foix, D., Berg, E.J., Rousse, G., Doublet, M.-L., Gonbeau, D., Novak, P., Van Tendeloo, G., et al. (2015). Visualization of O-O peroxo-like dimers in high-capacity layered oxides for Li-ion batteries. Science *350*, 1516–1521.

9. Sathiya, M., Rousse, G., Ramesha, K., Laisa, C.P., Vezin, H., Sougrati, M.T., Doublet, M.-L., Foix, D., Gonbeau, D., Walker, W., et al. (2013). Reversible anionic redox chemistry in high-capacity layered-oxide electrodes. Nat. Mater. *12*, 827–835.

10. Saubanère, M., McCalla, E., Tarascon, J.-M., and Doublet, M.-L. (2016). The intriguing question of anionic redox in high-energy density cathodes for Li-ion batteries. Energy Environ. Sci. *9*, 984–991.

11. Assat, G., Delacourt, C., Dalla Corte, D.A., and Tarascon, J.-M. (2016). Editors' Choice—Practical Assessment of Anionic Redox in Li-Rich Layered Oxide Cathodes: A Mixed Blessing for High Energy Li-Ion Batteries. J. Electrochem. Soc. *163*, A2965–A2976.

12. Assat, G., Iadecola, A., Foix, D., Dedryvère, R., and Tarascon, J.-M. (2018). Direct Quantification of Anionic Redox over Long Cycling of Li-Rich NMC via Hard X-ray Photoemission Spectroscopy. ACS Energy Lett. *3*, 2721–2728.

13. Ma, C., Alvarado, J., Xu, J., Clément, R.J., Kodur, M., Tong, W., Grey, C.P., and Meng, Y.S. (2017). Exploring Oxygen Activity in the High Energy P2-Type $Na_{0.78}Ni_{0.23}Mn_{0.69}O_2$ Cathode Material for Na-Ion Batteries. J. Am. Chem. Soc. *139*, 4835–4845.

14. Clément, R.J., Bruce, P.G., and Grey, C.P. (2015). Review—Manganese-Based P2-Type Transition Metal Oxides as Sodium-Ion Battery Cathode Materials. J. Electrochem. Soc. *162*, A2589–A2604.

15. Gonzalo, E., Han, M.H., Amo, J.M.L. del, Acebedo, B., Casas-Cabanas, M., and Rojo, T. (2014). Synthesis and characterization of pure P2- and O3-Na2/3Fe2/3Mn1/3O2 as cathode materials for Na ion batteries. J. Mater. Chem. A *2*, 18523–18530.

16. Lee, D.H., Xu, J., and Meng, Y.S. (2013). An advanced cathode for Na-ion batteries with high rate and excellent structural stability. Phys. Chem. Chem. Phys. *15*, 3304.

17. Yabuuchi, N., Kajiyama, M., Iwatate, J., Nishikawa, H., Hitomi, S., Okuyama, R., Usui, R., Yamada, Y., and Komaba, S. (2012). P2-type Nax [Fe1/2Mn1/2] O2 made from earth-abundant elements for rechargeable Na batteries. Nat. Mater. *11*, 512.

18. Du, K., Zhu, J., Hu, G., Gao, H., Li, Y., and Goodenough, J.B. (2016). Exploring reversible oxidation of oxygen in a manganese oxide. Energy Env. Sci *9*, 2575–2577.

19. Billaud, J., Singh, G., Armstrong, A.R., Gonzalo, E., Roddatis, V., Armand, M., Rojo, T., and Bruce, P.G. (2014). $Na_{0.67}Mn_{1-x}Mg_xO_2$ ($0 \leq x \leq 0.2$): a high capacity cathode for sodium-ion batteries. Energy Env. Sci *7*, 1387–1391.

20. Maitra, U., House, R.A., Somerville, J.W., Tapia-Ruiz, N., Lozano, J.G., Guerrini, N., Hao, R., Luo, K., Jin, L., Pérez-Osorio, M.A., et al. (2018). Oxygen redox chemistry without excess alkali-metal ions in Na2/3[Mg0.28Mn0.72]O2. Nat. Chem. *10*, 288–295.

21. Yabuuchi, N., Hara, R., Kubota, K., Paulsen, J., Kumakura, S., and Komaba, S. (2014). A new electrode material for rechargeable sodium batteries: P2-type $Na_{2/3}[Mg_{0.28}Mn_{0.72}]O_2$ with anomalously high reversible capacity. J Mater Chem A *2*, 16851–16855.

22. Dai, K., Wu, J., Zhuo, Z., Li, Q., Sallis, S., Mao, J., Ai, G., Sun, C., Li, Z., Gent, W.E., et al. (2019). High Reversibility of Lattice Oxygen Redox Quantified by Direct Bulk Probes of Both Anionic and Cationic Redox Reactions. Joule *3*, 518–541.

23. Song, B., Hu, E., Liu, J., Zhang, Y., Yang, X.-Q., Nanda, J., Huq, A., and Page, K. (2019). A novel P3-type $Na_{2/3}Mg_{1/3}Mn_{2/3}O_2$ as high capacity sodium-ion cathode using reversible oxygen redox. J. Mater. Chem. A *7*, 1491–1498.

24. Radin, M.D., Alvarado, J., Meng, Y.S., and Van der Ven, A. (2017). Role of Crystal Symmetry in the Reversibility of Stacking-Sequence Changes in Layered Intercalation Electrodes. Nano Lett. *17*, 7789–7795.

25. Vinckevičiūtė, J., Radin, M.D., and Van der Ven, A. (2016). Stacking-Sequence Changes and Na Ordering in Layered Intercalation Materials. Chem. Mater. *28*, 8640–8650.

26. Radin, M.D., and Van der Ven, A. (2016). Stability of Prismatic and Octahedral Coordination in Layered Oxides and Sulfides Intercalated with Alkali and Alkaline-Earth Metals. Chem. Mater. *28*, 7898–7904.

27. Sandré, E., Brec, R., and Rouxel, J. (1990). Phase transitions induced in layered host structures during alkali metal intercalation processes. J. Solid State Chem. *88*, 269–277.

28. Maintz, S., Deringer, V.L., Tchougréeff, A.L., and Dronskowski, R. (2016). LOBSTER: A tool to extract chemical bonding from plane-wave based DFT: Tool to Extract Chemical Bonding. J. Comput. Chem. *37*, 1030–1035.

29. Dronskowski, R., and Bloechl, P.E. (1993). Crystal orbital Hamilton populations (COHP): energy-resolved visualization of chemical bonding in solids based on density-functional calculations. J. Phys. Chem. *97*, 8617–8624.

30. Ben Yahia, M., Vergnet, J., Saubanère, M., and Doublet, M.-L. (2019). Unified picture of anionic redox in Li/Na-ion batteries. Nat. Mater. *18*, 496–502.

31. Bai, X., Sathiya, M., Mendoza-Sánchez, B., Iadecola, A., Vergnet, J., Dedryvère, R., Saubanère, M., Abakumov, A.M., Rozier, P., and Tarascon, J.-M. (2018). Anionic Redox Activity in a Newly Zn-Doped Sodium Layered Oxide P2-$Na_{2/3}Mn_{1-y}Zn_yO_2$ ($0 < y < 0.23$). Adv. Energy Mater., 1802379.

32. Sathiya, M., Leriche, J.-B., Salager, E., Gourier, D., Tarascon, J.-M., and Vezin, H. (2015). Electron paramagnetic resonance imaging for real-time monitoring of Li-ion batteries. Nat. Commun. *6*, 6276.

33. Mortemard de Boisse, B., Nishimura, S., Watanabe, E., Lander, L., Tsuchimoto, A., Kikkawa, J., Kobayashi, E., Asakura, D., Okubo, M., and Yamada, A. (2018). Highly Reversible Oxygen-Redox Chemistry at 4.1 V in $Na_{4/7-x}[\square_{1/7}Mn_{6/7}]O_2$ (□: Mn Vacancy). Adv. Energy Mater. *8*, 1800409.

34. Rong, X., Hu, E., Lu, Y., Meng, F., Zhao, C., Wang, X., Zhang, Q., Yu, X., Gu, L., Hu, Y.-S., et al. (2019). Anionic Redox Reaction-Induced High-Capacity and Low-Strain Cathode with Suppressed Phase Transition. Joule *3*, 503–517.

35. de la Llave, E., Talaie, E., Levi, E., Nayak, P.K., Dixit, M., Rao, P.T., Hartmann, P., Chesneau, F., Major, D.T., Greenstein, M., et al. (2016). Improving Energy Density and Structural Stability of Manganese Oxide Cathodes for Na-Ion Batteries by Structural Lithium Substitution. Chem. Mater. *28*, 9064–9076.

36. Rong, X., Liu, J., Hu, E., Liu, Y., Wang, Y., Wu, J., Yu, X., Page, K., Hu, Y.-S., Yang, W., et al. (2018). Structure-Induced Reversible Anionic Redox Activity in Na Layered Oxide Cathode. Joule *2*, 125–140.

37. Ong, S.P., Richards, W.D., Jain, A., Hautier, G., Kocher, M., Cholia, S., Gunter, D., Chevrier, V.L., Persson, K.A., and Ceder, G. (2013). Python Materials Genomics (pymatgen): A robust, open-source python library for materials analysis. Comput. Mater. Sci. *68*, 314–319.

38. Kresse, G., and Furthmüller, J. (1996). Efficient iterative schemes for *ab initio* total-energy calculations using a plane-wave basis set. Phys. Rev. B *54*, 11169–11186.

39. Kresse, G., and Joubert, D. (1999). From ultrasoft pseudopotentials to the projector augmented-wave method. Phys. Rev. B *59*, 1758–1775.

40. Perdew, J.P., Burke, K., and Ernzerhof, M. (1996). Generalized Gradient Approximation Made Simple. Phys. Rev. Lett. *77*, 3865–3868.

41. Grimme, S., Antony, J., Ehrlich, S., and Krieg, H. (2010). A consistent and accurate *ab initio* parametrization of density functional dispersion correction (DFT-D) for the 94 elements H-Pu. J. Chem. Phys. *132*, 154104.

42. Grimme, S., Ehrlich, S., and Goerigk, L. (2011). Effect of the damping function in dispersion corrected density functional theory. J. Comput. Chem. *32*, 1456–1465.

43. Dudarev, S.L., Botton, G.A., Savrasov, S.Y., Humphreys, C.J., and Sutton, A.P. (1998). Electron-energy-loss spectra and the structural stability of nickel oxide: An LSDA+U study. Phys. Rev. B *57*, 1505–1509.

44. Henkelman, G., Arnaldsson, A., and Jónsson, H. (2006). A fast and robust algorithm for Bader decomposition of charge density. Comput. Mater. Sci. *36*, 354–360.

45. Momma, K., and Izumi, F. (2008). *VESTA*: a three-dimensional visualization system for electronic and structural analysis. J. Appl. Crystallogr. *41*, 653–658.

46. Wang, L., Maxisch, T., and Ceder, G. (2006). Oxidation energies of transition metal oxides within the GGA + U framework. Phys. Rev. B *73*, 195107.

SUPPLEMENTARY INFORMATION

Theoretical framework for the structural stability of P2-Na-based layered phases during anionic redox

Theoretical framework for the structural stability of P2-layered Na-based electrodes during anionic redox

Jean Vergnet,[1,3] Matthieu Saubanère,[2,3] Marie-Liesse Doublet, [2,3] and Jean-Marie Tarascon[1,3]*

[1]*Collège de France, Chimie du Solide et de l'Énergie, UMR CNRS 8260, Paris, France*
[2]*Institut Charles Gerhardt, CNRS – Université de Montpellier, Place Eugène Bataillon, 34 095 Montpellier, France*
[3]*Réseau Français sur le Stockage Électrochimique de l'Énergie (RS_2E), FR5439, Amiens, France*

STRUCTURAL DESCRIPTION

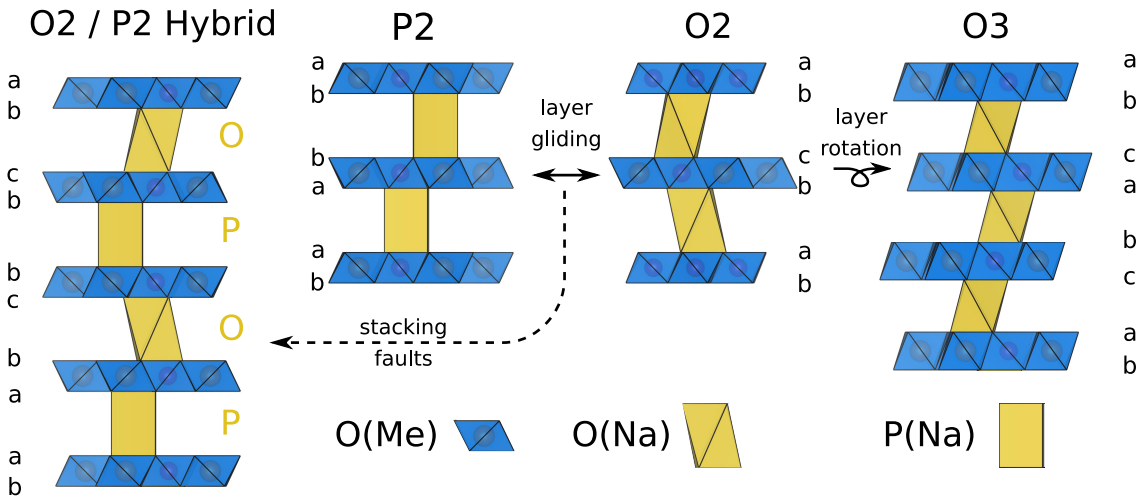

Figure S1: Stacking phases in Na-deficient compounds as classified by Delmas & al.[3]

The pristine material synthesized in P2, undergoes phase transition to O2 by a gliding of every other layer which preserves the covalent structure of the MnO_2 layers and induces a low activation barrier. The accumulation of stacking faults can be approximated by a regular hybrid stacking such as OP4. A transition from O2 to O3 requires a rotation of the O lattice which breaks the covalent Mn-O bonds, thus requiring a high activation energy.

ANIONIC REDOX IN MODEL COMPOUND

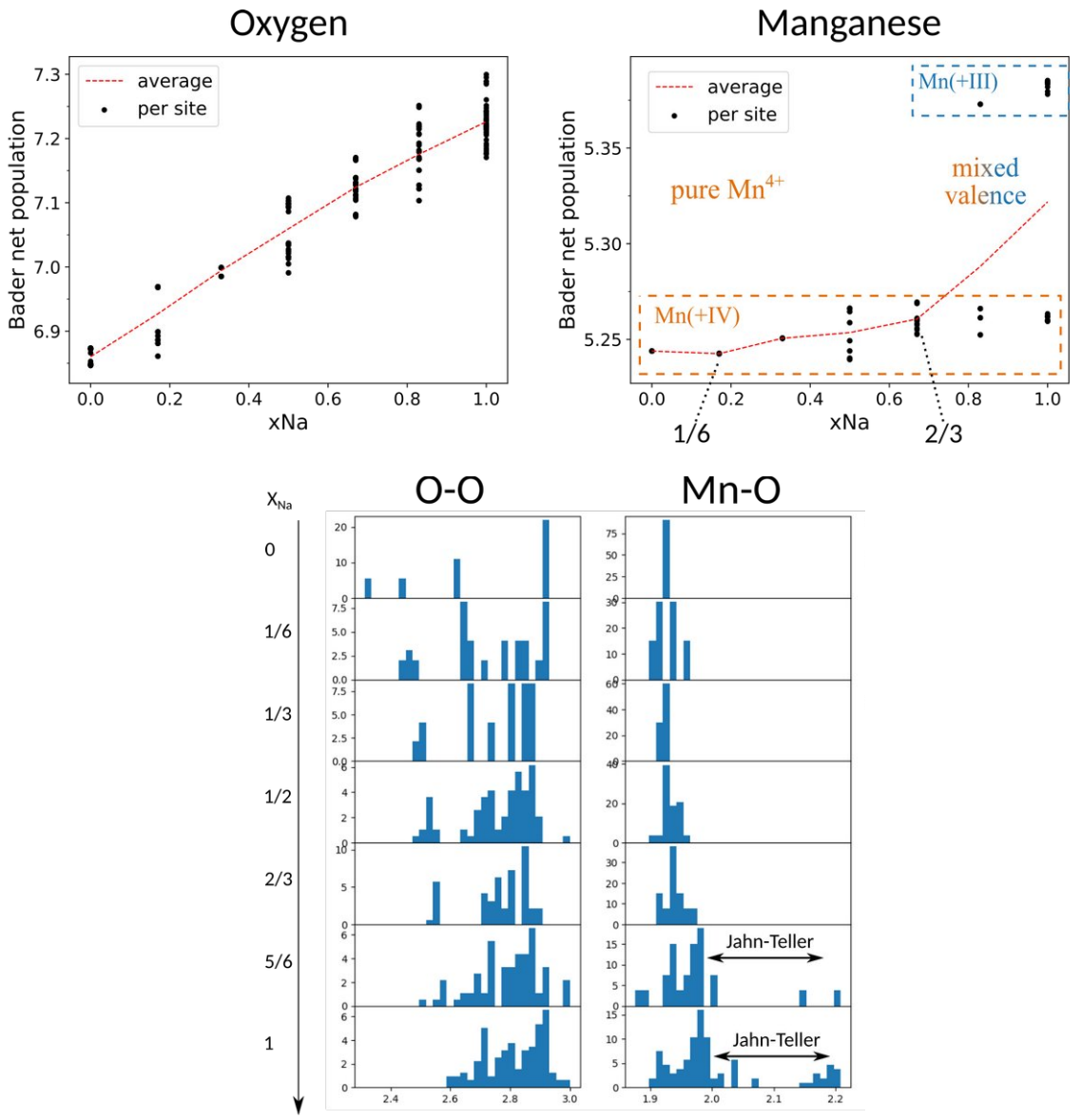

Figure S2: Top: Bader charge for O & Mn (by site) during charge
Bottom: Histogram of distance to the next neighbors during charge (in Å)

To ensure that our model structure correctly reproduces anionic redox, we generated desodiated structures (cf. Methods) and analyzed their Bader population and distance histogram. For x<2/3, the Bader populations on Mn sites, comparable to those of Mn^{4+} in Li_2MnO_3 (5.26), indicate that Mn stays +4 throughout charge (cf. Fig. S2.b) hence resulting in pure anionic oxidation. Conversely, upon discharge (x>2/3), some Mn sites have Bader populations comparable to Mn^{3+} in $LiMnO_2$ (5.38) thus indicating a mixed valence state of the Mn. The presence of Mn^{3+} leads to Jahn-Teller distorted structures (P'2) as seen in the distance histogram, which is coherent with experimental observations[17] and the pDOS. The overall changes of electron population in Na and Mg are negligible compared to those of oxygen and Mn. Thus this model structure correctly reproduces both electronic and structural evolutions reported for this compound.

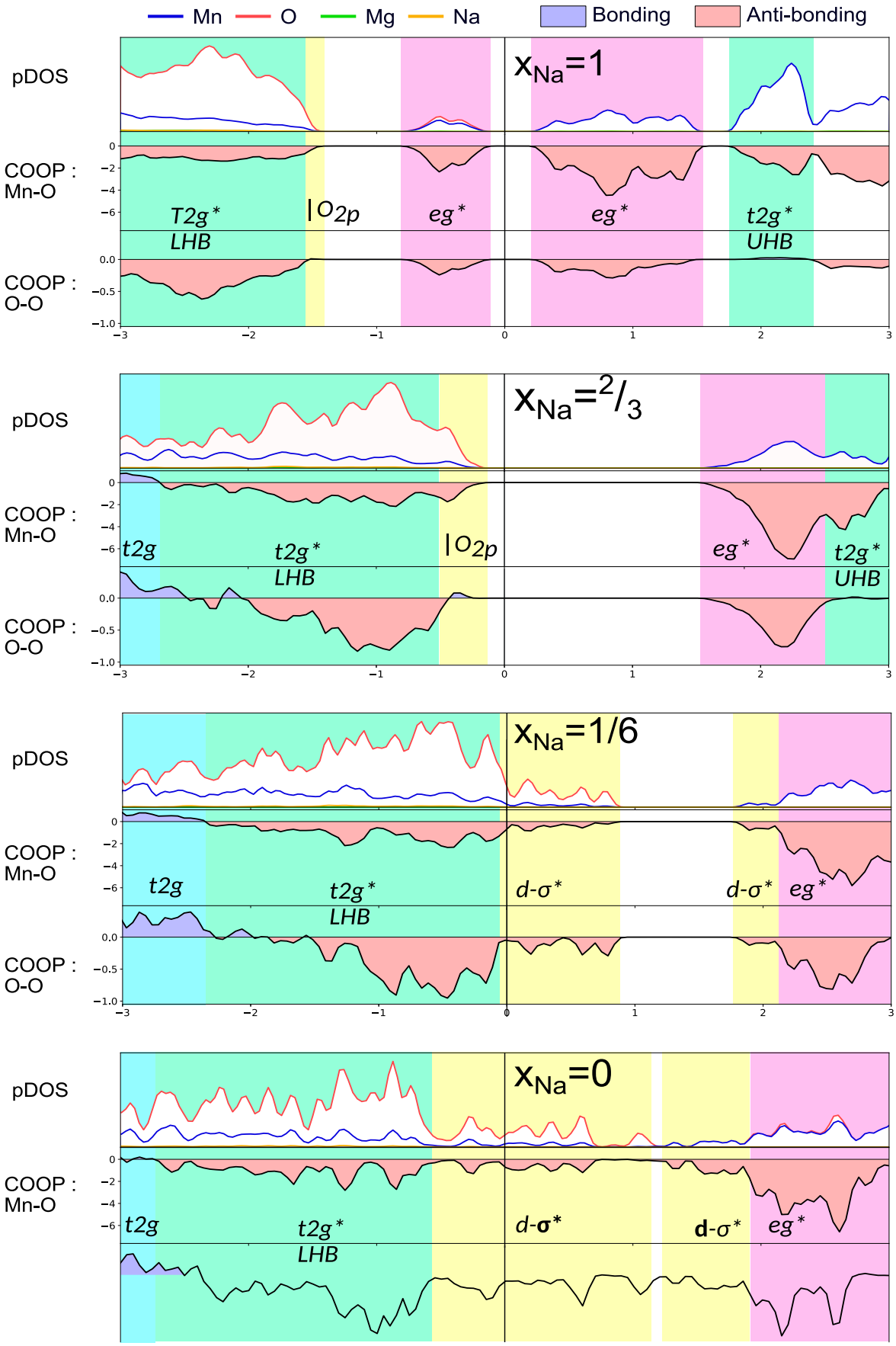
Mn
O
Mg
Na
Bonding
Anti-bonding
pDOS
COOP : Mn-O
COOP : O-O
x_{Na}=1
T2g*
LHB
O2p
eg*
eg*
t2g*
UHB
x_{Na}=2/3
t2g
t2g*
LHB
O2p
eg*
t2g*
UHB
x_{Na}=1/6
t2g
t2g*
LHB
d-σ*
d-σ*
eg*
x_{Na}=0
t2g
t2g*
LHB
d-σ*
d-σ*
eg*

Figure S3: Resolution of electronic structures of $Na_xMg_{1/3}Mn_{2/3}O_2$ using COOP for x=1, 2/3, 1/6 and 0 (from top to bottom). For each composition, the graph is composed of the Projected density of state (pDOS, above), the COOP of Mn-O bonds (middle) and the COOP of O-O pairs (bottom). Coulomb repulsion between d-electrons splits the MO^* band into Lower and Upper Hubbard Bands (noted LHB & UHB). Interestingly the empty e_g lies below the t_{2g}*^{UHB}, which is coherent with the high spin state generally observed for Mn^{3+} ($+4\mu_B$ local Mn magnetic moment). For x=1, Partially filled e_g^* LHB get split by the Jahn-Teller distortion of the MnO_6 octahedron. For x=2/3, non-bonding oxygen levels are visible just below the Fermi level. For x=1/6 and x=0, we observe a remixing of the metallic states with those of the formerly non-bonding oxygen, leading to a large dispersion at the Fermi level and at the bottom of the eg*.*

We remind that the analysis of crystal electronic levels (described by space groups) with molecular orbital levels (described by point groups) although very useful, is subject to caution and remains qualitative (especially when considering solid state effects such as the Hubbard splitting).

Electron Localization Function (ELF)

Non-bonding pairs

ELF is used to identify the regions of space where electron pairs are localized (i.e. not delocalized over M-O covalent bonds). Here, ELF isosurface forms two lobes around each oxygen, corresponding to non-bonding electron pairs, which point towards the Na layer and the Mg nuclei, respectively. Hence as for Na, the Mg reducing power preserve the non-bonding character of the oxygen electrons which form $|O_{2p}$ and $|O_{2s}$ lone pairs, hence clearly explaining the occurrence of anionic redox in alkali deficient compounds.

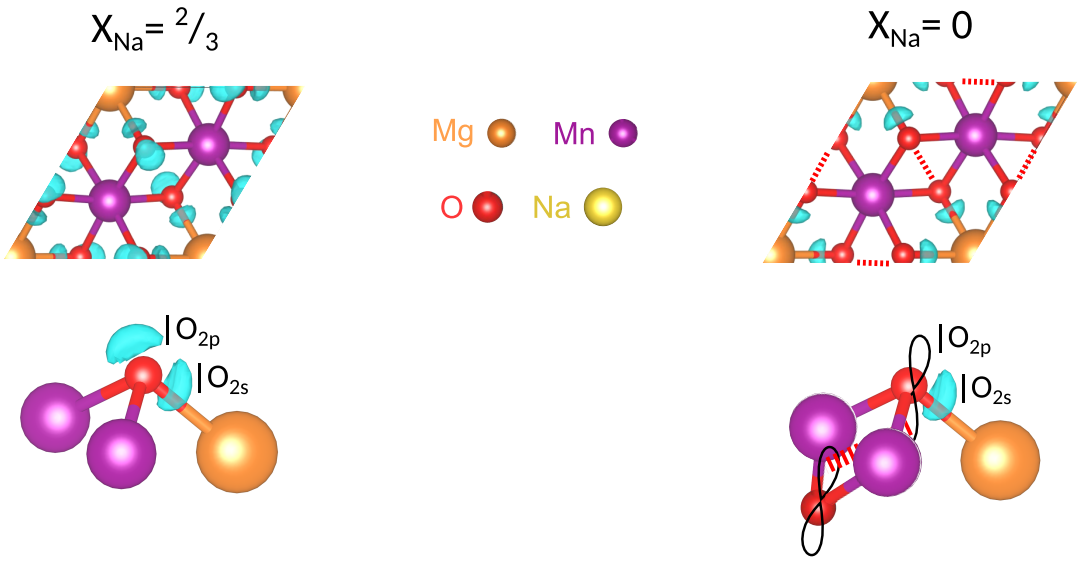

Figure S4: Molecular orbital description of oxygen geometry in $Na_xMg_{1/3}Mn_{2/3}O_2$ Crystal structure with zoom on oxygen, with E.L.F. isosurface locating non bonding doublets and insight from Lewis structure. Left : for x_{Na}=2/3 Right : x_{Na}=0. :

Ionicity & covalency in the structure

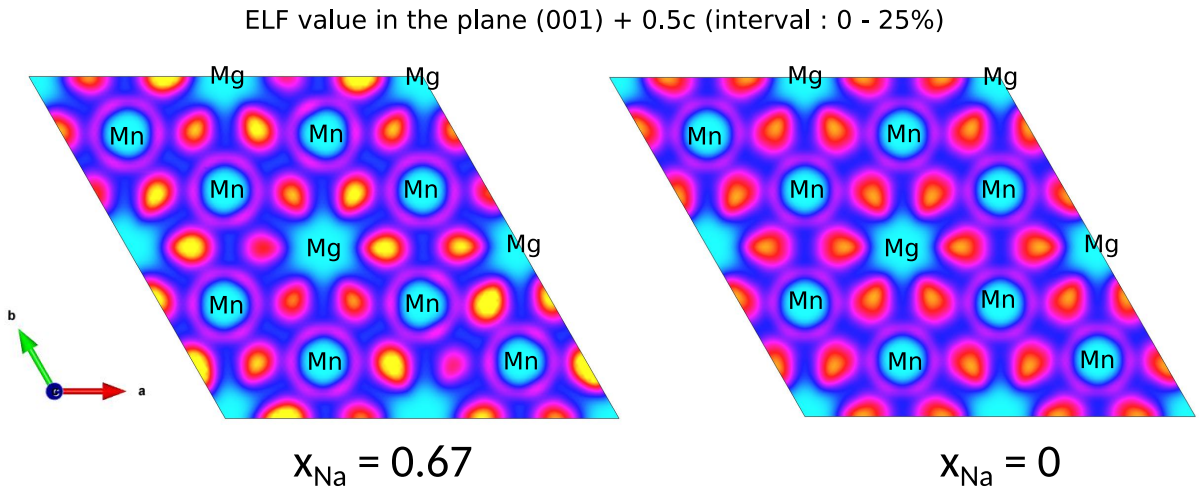

Figure S5: ELF value in the (001) plane for $Na_xMg_{1/3}Mn_{2/3}O_2$. Left : pristine (x = 2/3) , Right : End of charge (x=0). Interval : 0 % (cyan)– 25% (yellow) of maximum value.

Local maxima around a metal indicates a covalent bonding to the oxygen - Mn therefore appears as covalently bonded to the lattice while Mg-O bond are completely ionic (only valence electrons are considered in plane wave computation, which explains the absence of local mimima around Mg). As none of these two feature change when removing all Na, it qualitatively proves that neither Mn-O covalency nor Mg-O ionicity are impacted by the oxidation of oxygen.

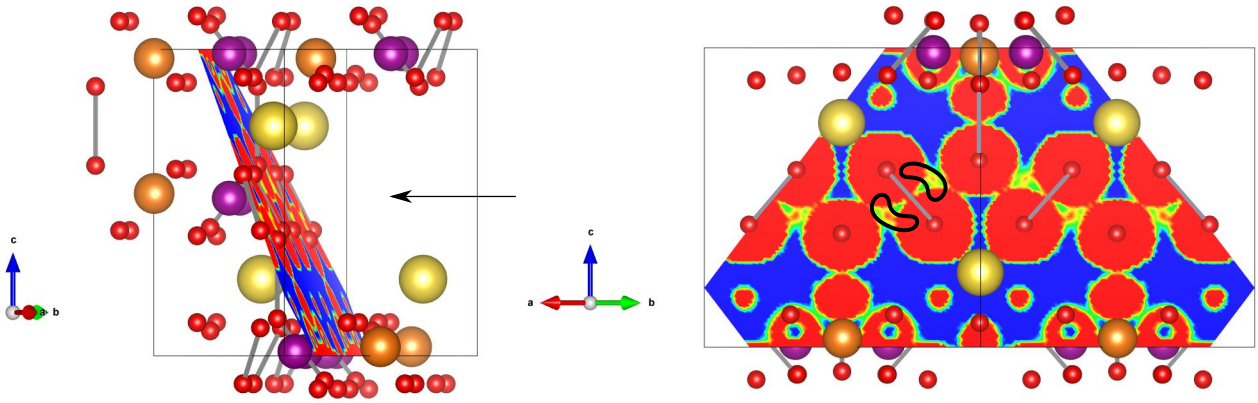

Figure S6: ELF value in a plane passing by the O-O pairs for $Na_{1/6}Mg_{1/3}Mn_{2/3}O_2$ (cooperative distortion). Interval : 0.4 % (blue) – 0.7% (red) of maximum value. Grey lines in the structures indicate short O-O distances (<2.5A)

Local maxima between oxygens (in black) indicates a (weak) covalent bonding between oxygen pairs even though the very low value of the maxima (0.055) indicates a very weak bonding, comparatively to the Mn-O bond.

O_2 RELEASE ENTHALPY

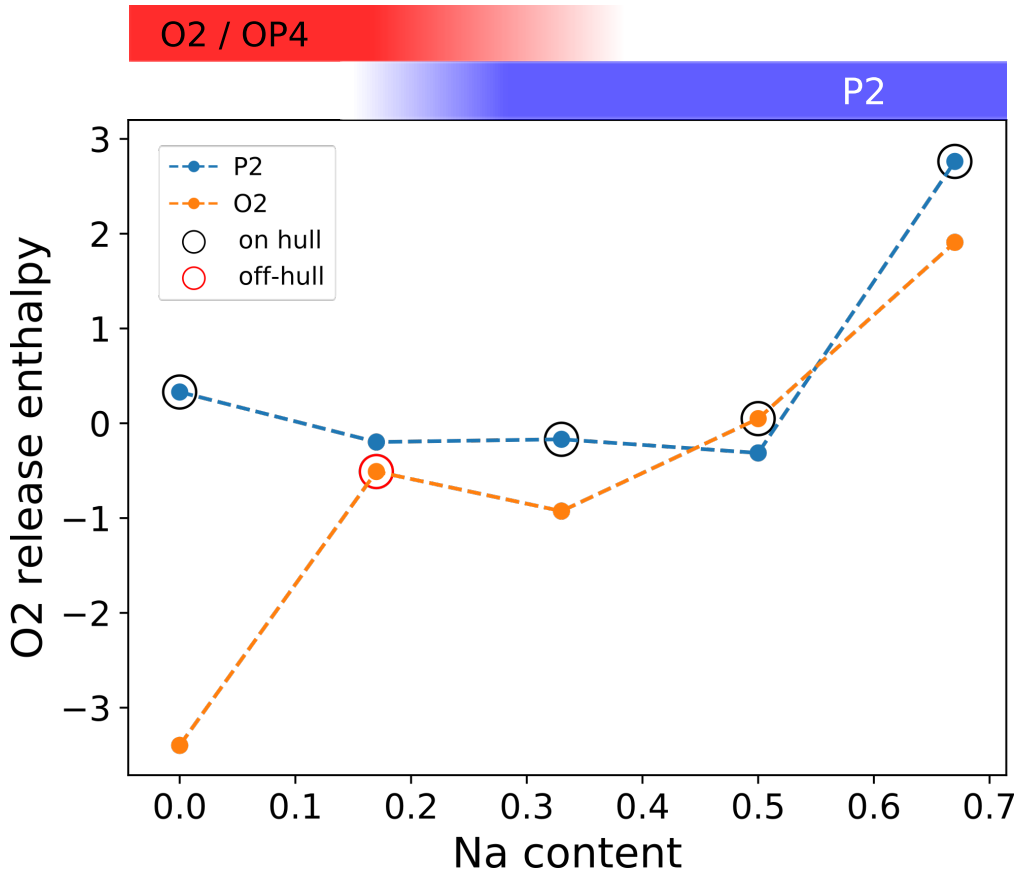

Figure S7: Enthalpy of O2 release reaction during anionic redox and phase stability. A negative enthalpy indicates a favorable release reaction, a positive value indicates a stability. A second order phase transition occurs between x=0.3 and x=0.1 Even though anionic redox destabilizes both stacking phases, the O2 phase is more prone to oxygen release than P2 phases, especially is we discard the off-hull point, added here for completeness.
For computational details, please refer to the Methods section, in the main text.

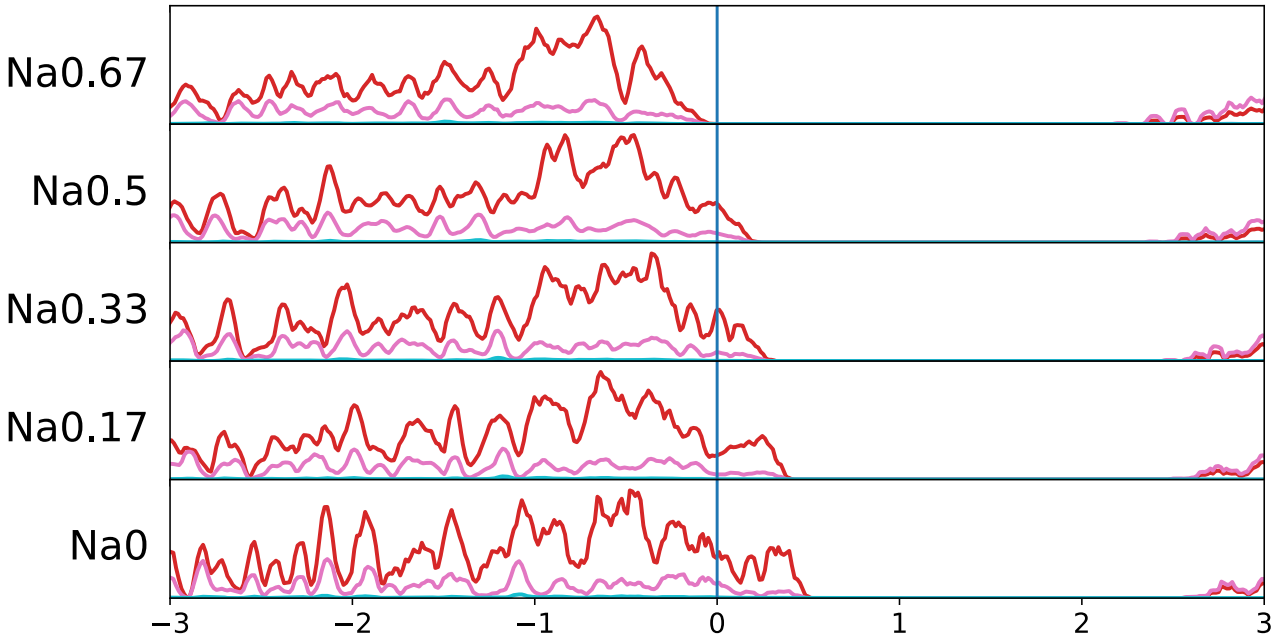

Figure S8: Single point calculation of Density of states (DOS) for $Na_xMg_{1/3}Mn_{2/3}O_2$ at various x, where the sodium content is given at the right of each DOS. Red curves curve stands for O while pink curves stands for Mn. The Fermi level is highlighted by a blue line.

Since no structural relaxation is performed, the Fermi level degeneracy is not lifted and the bandgap stays constant. This indicates that the lattice distortion is necessary to lift the degeneracy.

CHARGE AND SPIN DISTRIBUTION LINKED TO DISTORTION TYPES

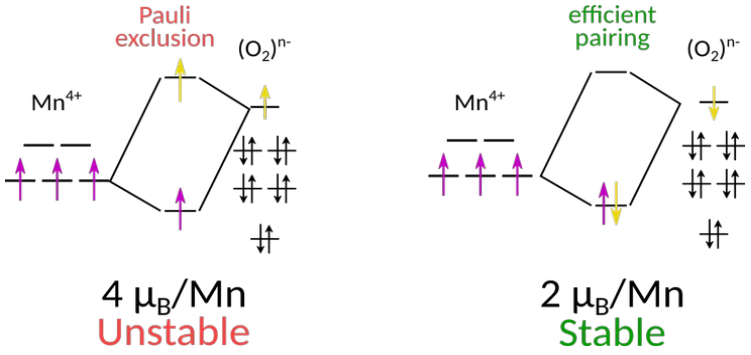

Figure S9: Effect of Oxygen spin state on the reductive coupling mechanism (RCM).
Parallel Mn and O spin configuration (left) is not stabilized by Mn-O_2 interaction.
Antiparallel configuration (right) allows efficient coupling and stabilization.
Thus RCM leads to spin decrease, as confirmed by bader charges, see below, fig. 10.

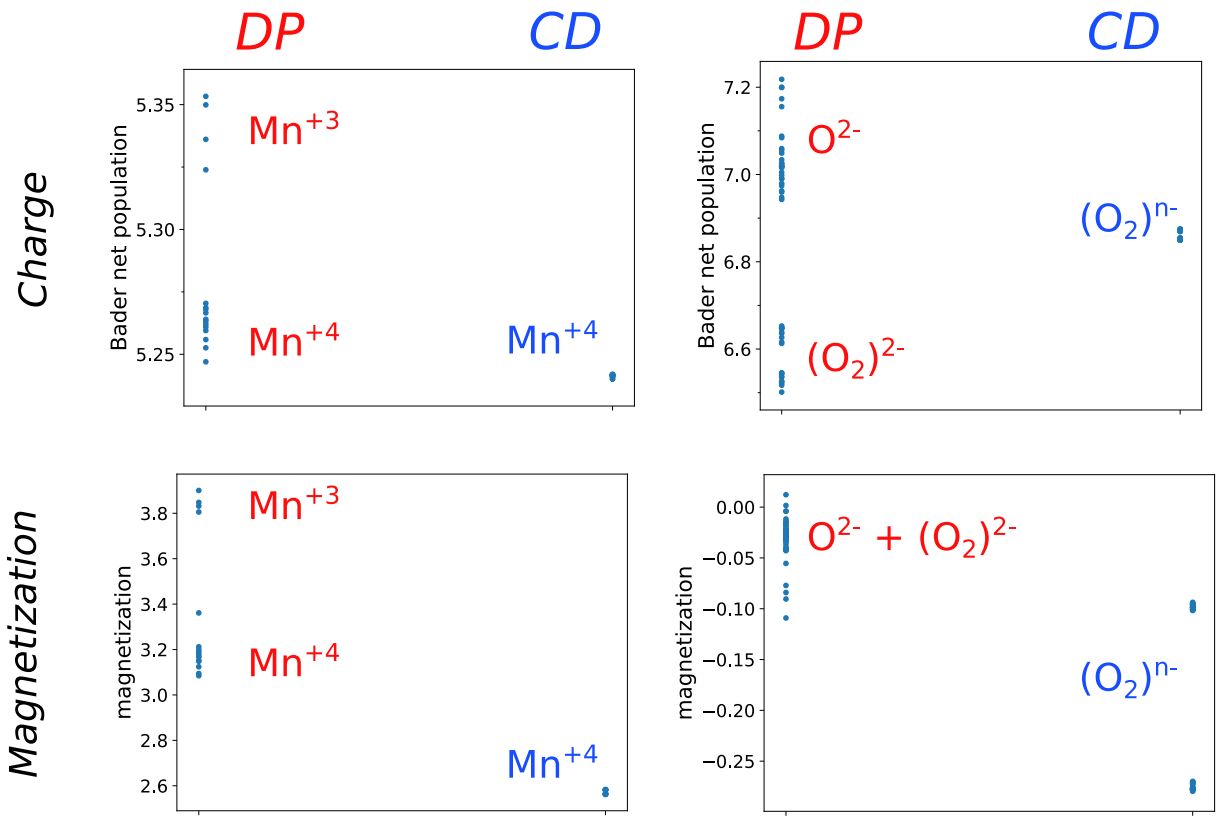

Figure S10: Comparison of Mn and O Bader population and magnetization at X_{Na}=0.17

During the Collective distortion (CD) due to RCM, Mn stays in +4 while oxygen are homogeneouly oxidized and magnetic (the two values -0.1 and -0.3 are due to spin contamination, cf. Methods). On the contrary, during disproportionation (DP), Oxygen population is splitted between oxo and peroxo species which are both non-magnetic. The electron lying in high-energy peroxo orbitals pour down into the metallic ones, leading to a reduction of the neighbor Mn into +3 state.

HYBRID STACKING AT THE END OF CHARGE

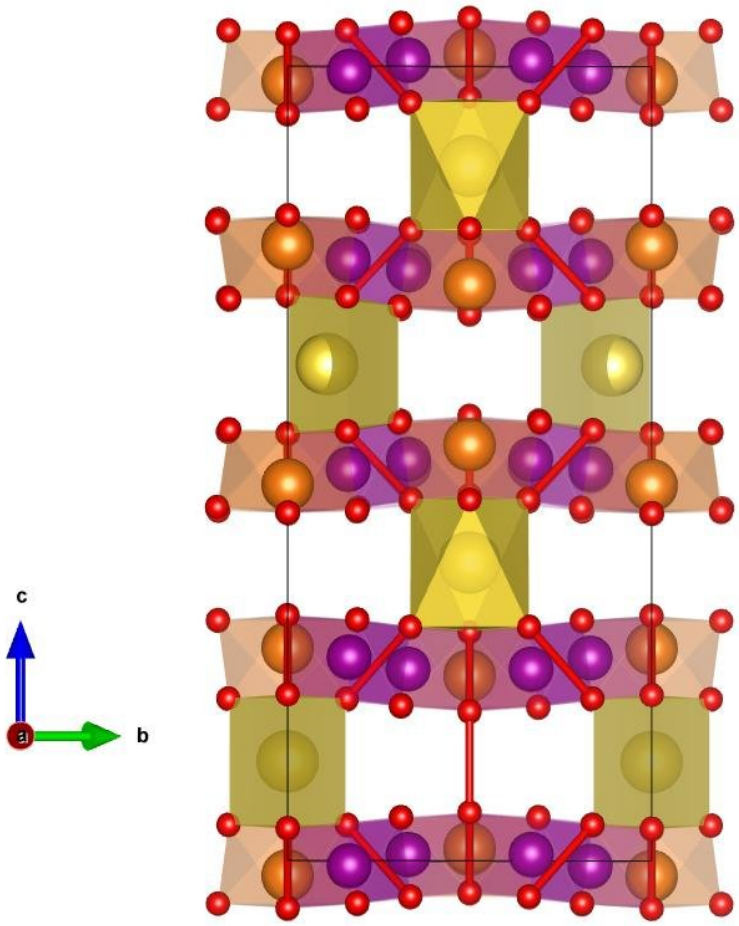

Figure S11: OP4 Structure

Corrugation along b* direction is stabilized by interlayer bonding in the prismatic inter-layers, thus providing a driving force for the ordering of Na in the layer.

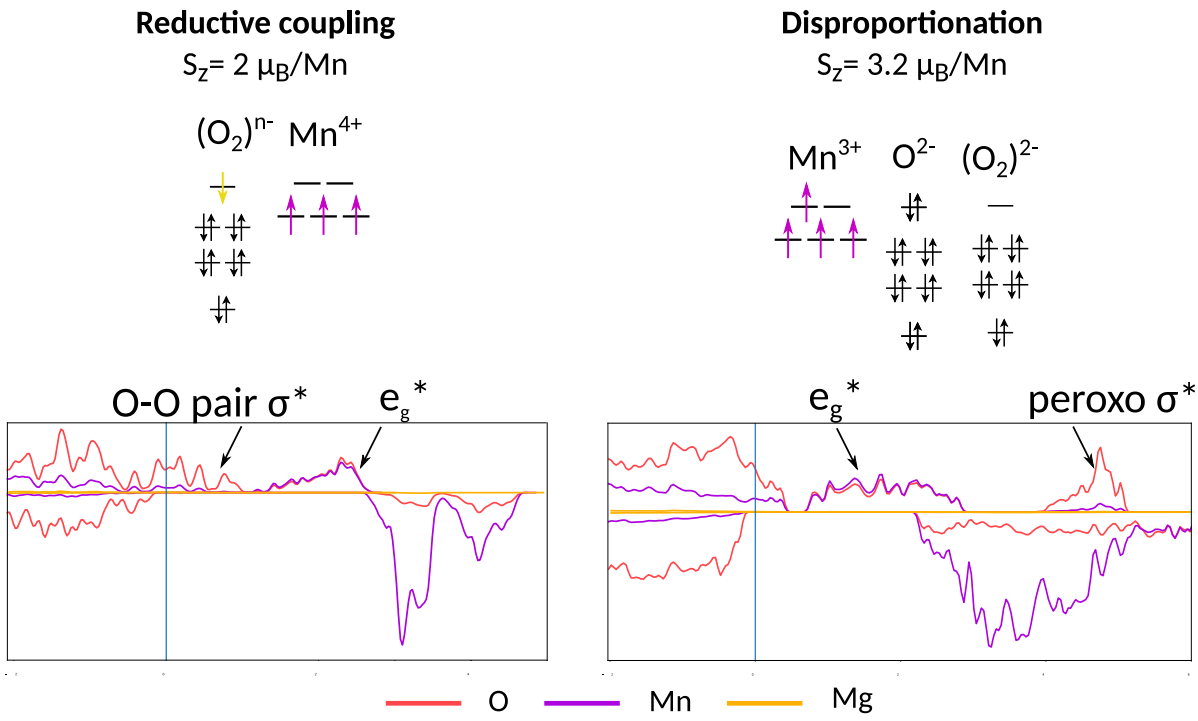

Figure S12: projected density of states for the two types of distortion corresponding to the structure of fig 6 in the main text. .

In the case of true peroxo formation, the uppermost empty oxygen states are raised above the Mn-O* states, thus leading to the reduction of metal upon discharge, which is the cause of hysteresis.

Partial Charge density analysis

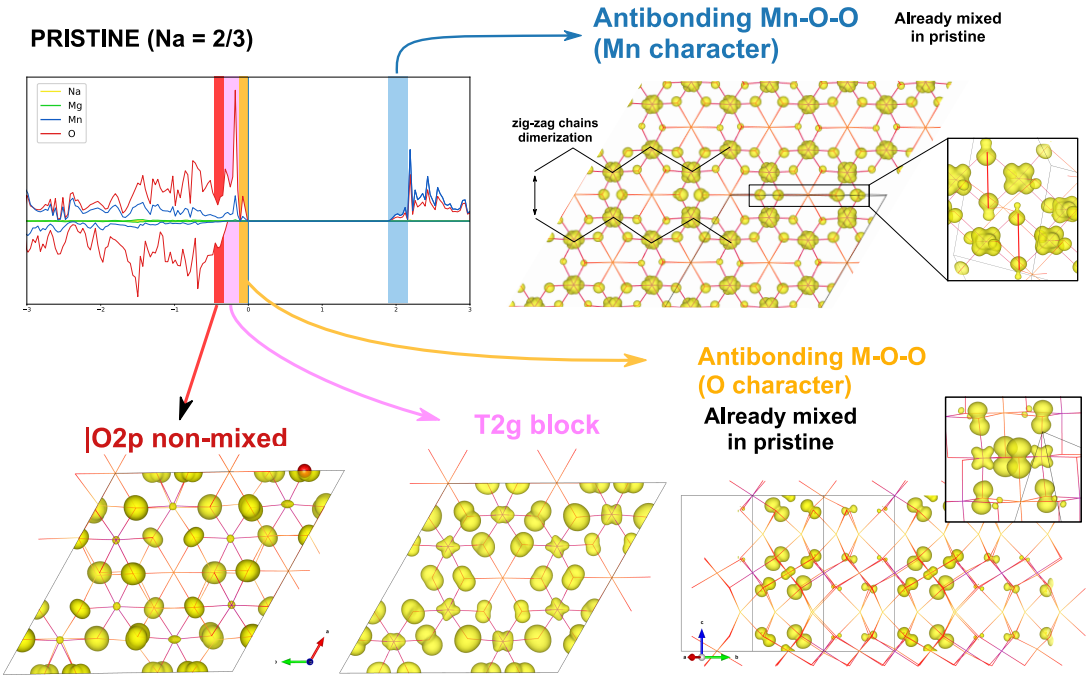

Figure S13: Analysis of the symmetry of electronic states near the band-gap in the pristine $Na_{2/3}Mg_{1/3}Mn_{2/3}O_2$: the electronic states lying within the energy range indicated in the pDOS (top left corner) are visualized using a Partial charge density projection (PARCHARG).

Description of each parcharg by increasing energy range (in eV, relative to E_{Fermi}):
Red : [-0.4, -0.3 eV] : Non-bonding $|O_{2p}$ states
Pink : [-0.3, -0.1 eV] : Mn-O states with t_{2g} symmetry
Orange : [-0.1, 0 eV] : cooperative orbital arrangement with high O weight and small Mn weight
Inset : magnification to show the interaction between O-O π-bonds and d orbitals
Blue : [1.90, 2.15 eV] : cooperative orbital arrangement with high Mn weight and small O weight
Inset : magnification to show the interaction between O-O σ-bonds and d orbitals

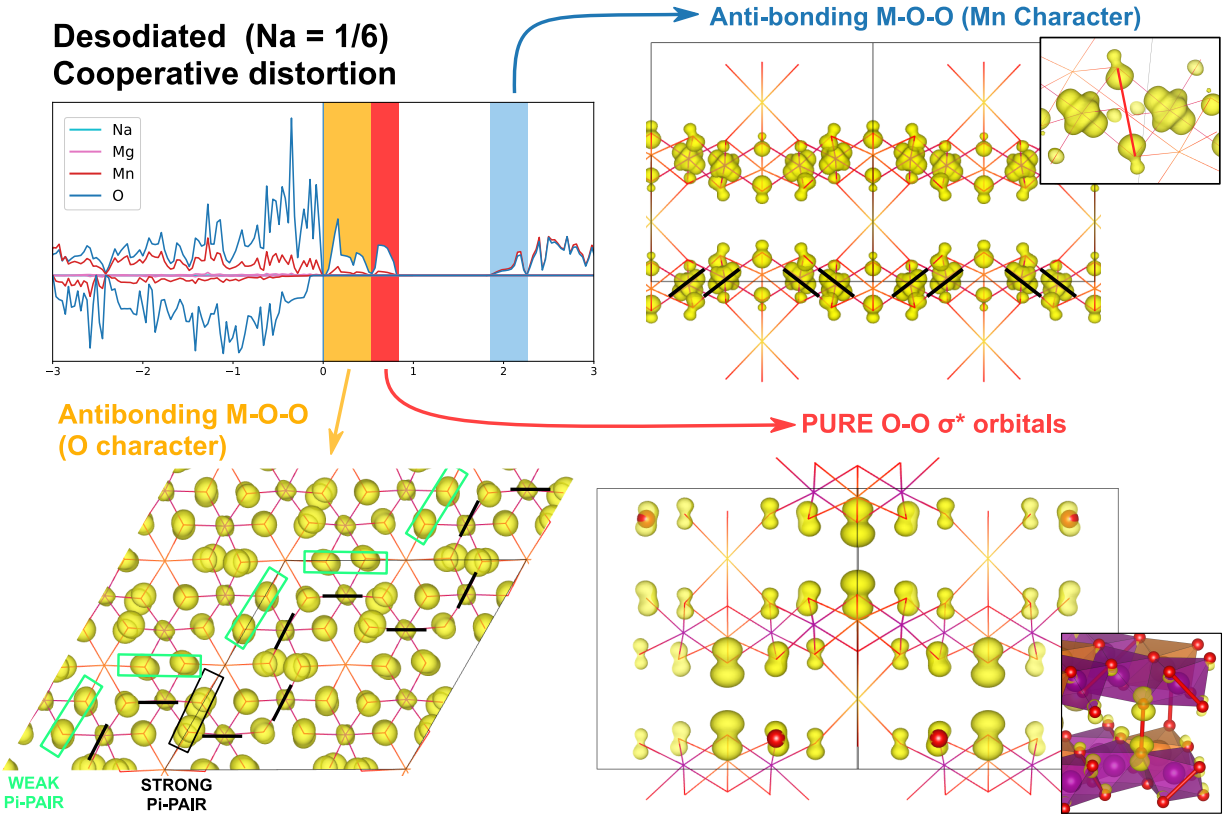

Figure S14: Analysis of the symmetry of empty states in the desodiated $Na_{1/6}Mg_{1/3}Mn_{2/3}O_2$: the electronic states lying within the energy range indicated in the pDOS (top left corner) are visualized using a Partial charge density projection (PARCHARG).

Description of each parcharg by increasing energy range (in eV, relative to E_{Fermi}):

Orange : [0, 0.53 eV] : cooperative orbital arrangement with high O weight and small Mn weight

Red : [0.53,0.81 eV] : Sigma anti-bonding , without any Mn participation*

Inset : magnification to show how the O_{2pz} orbitals follows a sigma symmetry

Blue : [1.80,2.25 eV] : cooperative orbital arrangement with high Mn weight and small O weight

Inset : magnification to show the interaction between O_{2pz} and d orbitals, similar to the pristine but with a larger hole population

SPIN ORDERING ENERGY AND PAIRING ENERGY

Figure S15:

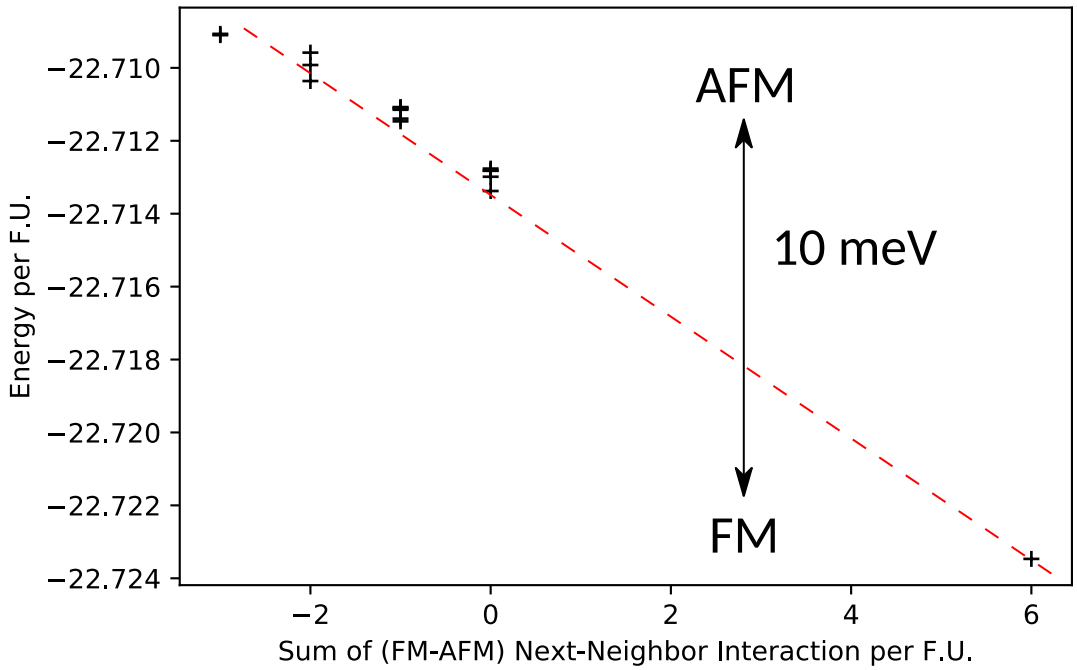

Energies of $Na_{2/3}Mg_{1/3}Mn_{2/3}O_2$ considering various magnetic orders as a function of the spin order parameter. The difference between antiferromagnetic and ferromagnetic order is around 10meV.

The spin order parameter is taken as the difference between the number of parallel and anti-parallel interaction between next neighbor Mn4+. Ferromagnetic order only has parallel interaction, so it spin order is the maximum (24). Anti-ferromagnetic orders have variable number of parallel and anti parallel. The linear dependence in the order parameter indicates that the spin interaction in this compound can be fitted within a 2D next neighbor Ising model.

As a comparison, the same structure after a Non-magnetic relaxation has an energy of **-20.71 eV/F.U.** which is 2eV per formula unit above the spin polarized structure, disregarding their spin order.